UCRL-TR-202300

LAWRENCE
LIVERMORE
NATIONAL
LABORATORY

Two-Parameter Failure Model Improves Time-Independent and Time-Dependent Failure Predictions

R.L. Huddleston

December 2003

This document was prepared as an account of work sponsored by an agency of the United States Government. Neither the United States Government nor the University of California nor any of their employees, makes any warranty, express or implied, or assumes any legal liability or responsibility for the accuracy, completeness, or usefulness of any information, apparatus, product, or process disclosed, or represents that its use would not infringe privately owned rights. Reference herein to any specific commercial product, process, or service by trade name, trademark, manufacturer, or otherwise, does not necessarily constitute or imply its endorsement, recommendation, or favoring by the United States Government or the University of California. The views and opinions of authors expressed herein do not necessarily state or reflect those of the United States Government or the University of California, and shall not be used for advertising or product endorsement purposes.

This work was performed under the auspices of the U.S. Department of Energy by University of California, Lawrence Livermore National Laboratory under Contract W-7405-Eng-48.

REPORT NUMBER........................

TWO-PARAMETER FAILURE MODEL IMPROVES TIME-INDEPENDENT AND TIME-DEPENDENT FAILURE PREDICTIONS

Roy L. Huddleston

December 2003

CONTENTS

Acknowledgements .... **viii**

Abstract .... **ix**

1.0 INTRODUCTION **1**

2.0 FAILURE MODES AND MODELS **3**

- 2.1 FAILURE MODES 3
- 2.2 CLASSICAL FAILURE MODELS 3

3.0 H2P FAILURE MODEL **6**

- 3.1 DETERMINING PARAMETER "b" FROM A SECOND FAILURE TEST 8
  - 3.1.1 Determining Parameter "b" from a Pure Compression Test 8
  - 3.1.2 Determining Parameter "b" from a Pure Torsion Test 9
- 3.2 DETERMINING PARAMETER "b" FROM A SET OF M FAILURE TESTS 10
- 3.3 MODEL FAILURE SURFACES 10

4.0 MODEL/DATA CORRELATIONS **14**

- 4.1 DATA SET 1 CORRELATIONS—PUGH ET AL. TENSION, COMPRESSION, AND TORSION TESTS OF CAST IRON UNDER HYDROSTATIC PRESSURE 14
  - 4.1.1 Scaling Data Set 1 15
  - 4.1.2 Principal Stresses and Stress Parameters 18
  - 4.1.3 Material Strength Properties 18
  - 4.1.4 H2P Model Parameter "b" 22
  - 4.1.5 Data Set 1: Model / Data Correlations 22
- 4.2 DATA SET 2 CORRELATIONS—CHANDLER AND MAIR TENSION AND COMPRESSION TESTS OF CAST IRON UNDER HYDROSTATIC PRESSURE 28
  - 4.2.1 Scaling Data Set 2 28
  - 4.2.2 Principal Stresses and Stress Parameters 29
  - 4.2.3 Material Strength Properties 30
  - 4.2.4 H2P Model Parameter "b" 30
  - 4.2.5 Data Set 2:Model/Data Correlations 31
- 4.3 DATA SET 3 CORRELATIONS—VON KARMAN TENSION AND COMPRESSION TESTS OF MARBLE UNDER HYDROSTATIC PRESSURE 31
  - 4.3.1 Scaling Data Set 3 33
  - 4.3.2 Principal Stresses and Stress Parameters 34
  - 4.3.3 Material Strength Properties and H2P Model Parameter "b" 35
  - 4.3.4 Data Set 3: Model/Data Correlations 36
- 4.4 DATA SET 4 CORRELATIONS—CHUBB AND BOLTON BIAXIAL CREEP-RUPTURE TESTS OF TYPE 316 STAINLESS STEEL 36
  - 4.4.1 Biaxial Creep-Rupture Data 37
  - 4.4.2 Methodology for Predicting Creep-Rupture 38
  - 4.4.3 Data Set 5: Data/Model Correlations 39
- 4.5 CREEP-FATIGUE LIFE PREDICTION METHODOLOGY 40
  - 4.5.1 Current Methodology 43
    - 4.5.1.1 Linear Damage Model 43

4.5.1.2 Mises Equivalent Stress Model 45
4.5.1.3 Bilinear Creep-Fatigue Damage Interaction Diagram 45
4.5.2 Proposed Modification to Creep-Fatigue Life Prediction Methodology 45
4.5.2.1 Bilinear Diagram Intersection Point 48
4.5.2.2 H2P Model Determining Parameter "b" 50
4.5.3 Potential for Improved Creep-Fatigue Life Predictions 53

5.0 SUMMARY AND CONCLUSIONS 56

6.0 RECOMMENDATIONS 58

REFERENCES 59

APPENDIX A. LEAST-SQUARES METHOD FOR DETERMINING H2P MODEL PARAMETER "b" FOR A SET OF M TIME-INDEPENDENT FAILURE TESTS 60

APPENDIX B. LEAST-SQUARES METHOD FOR DETERMINING H2P MODEL PARAMETER "b" FOR A SET OF M CEH-TYPE, CREEP-FATIGUE TESTS 63

NOMENCLATURE 67

DISTRIBUTION 70

LIST OF FIGURES

Page

Figure 2.1. Principal and deviatoric stresses. 5

Figure 3.1. Geometric representation of H2P failure model stress parameters. 7

Figure 3.2. Comparison of 2-D failure contours. 11

Figure 3.3. H2P model failure surface (ratio of compressive to tensile strength of 1.75 [b = 0.28]) 12

Figure 3.4. Mises and Tresca 3-D failure surfaces 13

Figure 3.5. Rankine model 3-D failure surface 13

Figure 4.1. Tensile or shear stress at fracture versus volumetric compressive stress 17

Figure 4.2. Comparison of predicted and observed tensile stress, Z, at fracture for tests of cast iron conducted under combined axial tension, Z, and hydrostatic pressure, P (H2P model parameter “b” determined by pure compression tests) 26

Figure 4.3. Comparison of predicted and observed torsional stress, W, at fracture for tests of cast iron conducted under combined torsion, W, and hydrostatic pressure, P (H2P model parameter “b” determined by pure compression tests). 26

Figure 4.4. Comparison of predicted and observed tensile stress, Z, at fracture for tests of cast iron conducted under combined tension, Z, and hydrostatic pressure, P (H2P model parameter “b” determined by a pure torsion test). 27

Figure 4-5. Comparison of predicted and observed torsional stress, W, at fracture for tests of cast iron conducted under combined torsion, W, and hydrostatic pressure, P (H2P model parameter “b” determined by a pure torsion test). 27

Figure 4.6. Maximum normal stress versus volumetric stress for cylindrical, cast-iron specimens tested under combined tension or compression and hydrostatic pressure (Source: Chandler, Ref. 7, and Chandler and Mair, Ref. 8). 30

Figure 4.7. Comparison of predicted and observed tensile stress, Z, at fracture for cylindrical, cast-iron specimens tested under combined tension, Z, and hydrostatic pressure, P (H2P model parameter “b” determined by pure compression test). 32

Figure 4.8. Comparison of predicted and observed compressoion stress, Z, at fracture for cylindrical, cast-iron specimens tested under combined compression, Z, and hydrostatic pressure, P (H2P model parameter “b” determined by compression test). 32

Figure 4.9. T. von Karman failure tests of marble cylinders under combined axial compression and hydrostatic pressure [Source: Nadai, A., Theory of Flow and Fracture of Solids, McGraw-Hill Book Company, Inc., New York, 1950, pp. 239-244]. 33

Figure 4.10. Comparison of predicted and observed axial stress, Z, at fracture for marble cylinders tested under combined compression, Z, and hydrostatic pressure, P (H2P model parameter “b” determined by pure compression test) 36

Figure 4.11. Correlation of 316 stainless-steel biaxial stress-rupture data with 2-D isochronous stress-rupture contours. 39

Figure 4.12. Correlation of the ratio of predicted-to-observed life with stress state based on the H2P failure model. 41
Figure 4.13. Correlation of the ratio of predicted-to-observed life with stress state based on the Mises failure model........ 41
Figure 4.14. Correlation of the ratio of predicted-to-observed life with stress state based on theTresca failure model. 42
Figure 4.15. Correlation of the ratio of predicted-to-observed life with stress state based on the Rankine failure model. 42
Figure 4.16. Bilinear creep-fatigue interaction diagram. 44
Figure 4.17. Cyclic stress-strain behavior for TEH and CEH cycles........ 46

LIST OF TABLES

Page

Table 4.1 Data Set 1: scaled data. 16

Table 4.2. Data Set 1: applied stress loadings at fracture. 19

Table 4.3. Equations for principal stresses and stress parameters for three basic loading conditions of cylindrical specimens 20

Table 4.4 Data Set 1: applied loadings and stre ss parameters 21

Table 4.5. Equations for predicting the applied stress necessary to produce fracture based on the Mises, Tresca, Rankine, and H2P failure models 24

Table 4.6. Data Set 1: comparison of predicted and observed fracture stress. 25

Table 4.7. Data Set 2: Chandler and Mair fracture results for cylindrical, cast-iron specimens tested under combined tension or compression and hydrostatic pressure. 29

Table 4.8. Applied loadings at "failure" for cylindrical specimens of marble tested under combined axial compression, Z, and hydrostatic pressure, P, by T. von Karman 35

Table 4.9. Data Set 4: biaxial creep-rupture of annealed Type 316 stainless-steel cylindrical specimens tested at 1112°F (600°C) in air by Chubb and Bolton 37

Table 4.10. Data Set 4: *averaged* biaxial creep-rupture data of annealed Type 316 stainless-steel cylindrical specimens tested at 1112°F (600°C) in air by Chubb and Bolton 38

Table 4.11. Creep-fatigue data utilized in demonstrating H2P failure model applicability to creep-fatigue failure prediction 54

Table 4.12. A comparison of predicted and observed creep-fatigue lives based on the H2P model versus the Mises equivalent stress model 55

ACKNOWLEDGMENTS

The author wishes to acknowledge and thank Marc Costantino and the Lawrence Livermore National Laboratory for their making this publication possible. The author also wishes to thank John G. Merkle, Oak Ridge National Laboratory, and Dr. John Landes, University of Tennessee, for reviewing the draft report and providing valuable input. The efforts of N. M. Sanford, Bev Chamberlain, and the Lawrence Livermore National Laboratory Technical Information Department are gratefully acknowledged in the editing and publication of the report

ABSTRACT

A new analytical model for predicting failure under a generalized, triaxial stress state was developed by the author and initially reported in 1984. The model was validated for predicting failure under elevated-temperature creep-rupture conditions. Biaxial data for three alloy steels, Types 304 and 316 stainless steels and Inconel 600, demonstrated two to three orders of magnitude reduction in the scatter of predicted versus observed creep-rupture times as compared to the classical failure models of Mises, Tresca, and Rankine. In 1990, the new model was incorporated into American Society of Mechanical Engineers (ASME) Code Case N47-29 for design of components operating under creep-rupture conditions. The current report provides additional validation of the model for predicting failure under time-independent conditions and also outlines a methodology for predicting failure under cyclic, time-dependent, creep-fatigue conditions. The later extension of the methodology may have the potential to improve failure predictions there as well. These results are relevant to most design applications, but they have special relevance to high-performance design applications such as components for high-pressure equipment, nuclear reactors, and jet engines.

1.0 INTRODUCTION

The purpose of this report is to summarize the results of work to extend the applicability of a failure model (strength theory) developed by the author to improve predictions both under time-dependent and time-independent failure conditions. The model can provide significantly improved failure predictions as compared to the classical models of von Mises (noted hereafter as Mises), Tresca, and Rankine.[1] One of the more important features of the model is that it has the capability to distinguish between tensile and compressive stress states in predicting failure, a feature that is lacking in the classical failure models that are utilized in most structural design codes today. The classical models are, in general, one-parameter models in that they use only failure under a pure tensile stress state to predict failure under other arbitrary, triaxial, stress states. The author's model is a two-parameter model that utilizes failure under two independent stress states (pure tension and one other stress state such as pure compression or pure torsion) to predict failure under other arbitrary triaxial stress states. The author's model is denoted in this report as the H2P (Huddleston two-parameter) model.

The H2P failure model was developed by the author in the mid-1980s.[2] This initial work was performed while the author was employed by Oak Ridge National Laboratory (ORNL), Oak Ridge, Tennessee, and was sponsored by the U.S. Department of Energy. The work focused on development and validation of improved design and failure criteria for nuclear reactor components operating at elevated temperature. The H2P model demonstrated significantly improved failure predictions for Type 304 stainless steel specimens tested to failure at 1100°F (593°C) under biaxial stress conditions. The model reduced the variability between predicted and observed lives by two to three orders of magnitude. In 1990, the American Society of Mechanical Engineers (ASME) incorporated the model into ASME Code Case N47-29[3] for application in computing creep-rupture damage in components operating at elevated temperature. In 1992, the model was shown to provide significantly improved failure predictions for Type 316 stainless steel specimens tested under biaxial creep-rupture conditions at 1112°F (600°C);[4] and subsequently in 1993, the model was shown to provide analogous results for Inconel 600 tested at 1500°F (816°C).[5]

Because of insufficient program funds and other priorities, work on the H2P model at ORNL was terminated in the post-1993 period. In 1994, the author retired from ORNL, and realizing the significant impact that the improved model could have in providing a more accurate design methodology, the author chose to continue to develop the methodology. The objective was to extend the applicability of the model to time-independent failure and to time-dependent creep-fatigue failure. This report documents this work and demonstrates the superior failure prediction capability of the H2P model as compared to the classical (one-parameter) failure models. The balance of this report provides: (1) a brief overview of the classical failure models; (2) a mathematical and geometric description of the H2P failure model; (3) model/data correlations encompassing both time-independent and time-dependent failure under biaxial and triaxial stress states; and (4) some conclusions with recommendations for further model validation. The following sign convention is utilized for all stress parameters in this report: Tensile stresses are always positive, and compressive stresses (including pressure) are always negative.

2.0 FAILURE MODES AND MODELS

Methodologies for predicting failure address a specific failure mode. Given a specific failure mode, the predictive methodology generally combines a failure (strength) model, such as the Mises model, with other criteria, such as a damage accumulation criterion, for predicting failure. It is not the purpose of this document to review these modes and predictive methodologies in detail; however, a brief review of failure modes and selected failure models is provided as they relate to the current work. The major approaches to predicting failure are based on (1) crack initiation and (2) crack growth (unstable propagation). The models and assessments in this report are based on the crack-initiation approach. It is also assumed that stress-strain is predominately elastic such that true stress and engineering stress are approximately equal.

2.1 FAILURE MODES

Structural failure can occur by (1) time-independent modes, such as instantaneous or short-time fracture, plastic instability, fatigue, and instantaneous buckling, or (2) time-dependent modes such as creep-rupture, creep-fatigue, and creep-buckling. Various methods are used for predicting failure for each of these different modes. In each case, a failure model, such as the Tresca, Mises, or Rankine model, is generally factored into the overall predictive methodology. As previously noted, the H2P failure model has been shown to significantly improve life predictions for creep-rupture tests conducted under biaxial stress states.[2,4,5] In addition, the author has investigated the ability of the model to predict the onset of plastic instability for tensile loading under hydrostatic pressure and found that it provides significantly better predictions than the classical model of Mises. These unpublished results are not included in the current report. In this report, the applicability of the author's failure model for predicting three different failure modes is investigated; these modes are (1) time-independent fracture, (2) time-dependent stress-rupture, and (3) time-dependent creep-fatigue.

2.2 CLASSICAL FAILURE MODELS

A failure model, in general, provides an analytical means for converting a complex, three-dimensional (3-D), stress state into an equivalent uniaxial tensile stress state such that simple laboratory test data can be utilized to predict failure under complex, three-dimensional, stress states. The three most widely used failure models for structural design are: (1) the Tresca model (based upon constant maximum shear stress at failure); (2) the Mises model (based on constant elastic distortion strain energy at failure, which is equivalent to constant octahedral shear stress at failure); and (3) the Rankine model (based on constant maximum principal stress at failure).[1] These three phenomenological models are single-parameter models in the sense that they each are formulated to identically fit only one point in triaxial stress/failure space, this point generally being the uniaxial tensile failure point. Failure at any other arbitrary point in triaxial stress/failure space can then be predicted by the model. Mathematically, these three models can each be expressed in terms of one or more of the principal stresses. Given a complex stress state with ordered principal stresses $\sigma_1 \geq \sigma_2 \geq \sigma_3$, the equivalent stress intensity, σ_e, for these three models can be expressed by the equations:

$$\text{Tresca:} \quad \sigma_e = A_1(\sigma_1 - \sigma_3)\,, \tag{2.1}$$

$$\text{Mises:} \quad \sigma_e = A_2\sqrt{\frac{(\sigma_1 - \sigma_2)^2 + (\sigma_2 - \sigma_3)^2 + (\sigma_3 - \sigma_1)^2}{2}}\,, \tag{2.2}$$

and

$$\text{Rankine:} \quad \sigma_e = A_3\,\sigma_1 \tag{2.3}$$

where the A_1, A_2, and A_3 are constants that are determined such that the model identically fits a selected point in triaxial stress space. By selecting that point as the uniaxial tensile failure point, the equivalent stress intensity as defined by these three classical models becomes:

$$\text{Tresca:} \quad \sigma_e = (\sigma_1 - \sigma_3)\,, \tag{2.4}$$

$$\text{Mises:} \quad \sigma_e = \sqrt{\frac{(\sigma_1 - \sigma_2)^2 + (\sigma_2 - \sigma_3)^2 + (\sigma_3 - \sigma_1)^2}{2}}\,, \tag{2.5}$$

and

$$\text{Rankine:} \quad \sigma_e = \sigma_1 \tag{2.6}$$

Letting σ_0 denote the uniaxial tensile failure stress, then failure for any complex triaxial stress state is predicted to occur when σ_e equals σ_0.

The Rankine model can also be applied for compression stress states to limit the minimum principal stress to the material compression strength. Limiting both the maximum and minimum principal stresses to the tensile and compression strength of the material requires two independent Rankine failure equations, however. Equation 2.6 limits maximum principal stress to the material tensile strength. The analogous equation, equating σ_e to σ_3, defines failure when σ_3 equals σ, where σ denotes the failure stress under pure compression.

Principal stresses for an arbitrary structural element are depicted in Fig. 2.1a. The principal stresses can be broken down into the deviatoric stresses plus a hydrostatic stress component as depicted in Fig. 2.1b. The Rankine failure model is one-dimensional in that it relates failure to only one of the three principal stresses (σ_1); thus, the remaining two principal stresses have no influence on failure. While some materials behave in this manner, most do not. The Tresca model is two-dimensional in that it relates failure to the difference between only two of the maximum and the minimum principal stresses (σ_1 and σ_3). The difference between any two of the principal stresses is equivalent to the difference between the analogous two deviatoric stresses, which eliminates any influence of the hydrostatic stress. The Tresca model, therefore, allows no influence on failure by the intermediate principal stress or the hydrostatic stress. Failure for many materials can be reliably predicted using the Tresca model; however, under certain conditions, such as triaxial stress states where there is a significant hydrostatic stress component, predictions may be inaccurate, as will be shown subsequently in this report. The Mises model is three-dimensional in the sense that it incorporates all three principal stresses; however, they are incorporated as differences between the principal stresses, which is equivalent to differences between the analogous deviatoric stresses. The Mises model thus allows the three deviatoric stresses to influence failure, but not the hydrostatic stress. Failure in many materials can be reliably predicted by the Mises model; however, because it does not account for the influence of the hydrostatic stress, it can result in inaccurate failure predictions where triaxial stresses are significant, as will be show subsequently. The H2P failure model, which is the subject of this report, is three-dimensional in that it allows all three principal stresses as well as the hydrostatic stress component to influence the failure prediction.

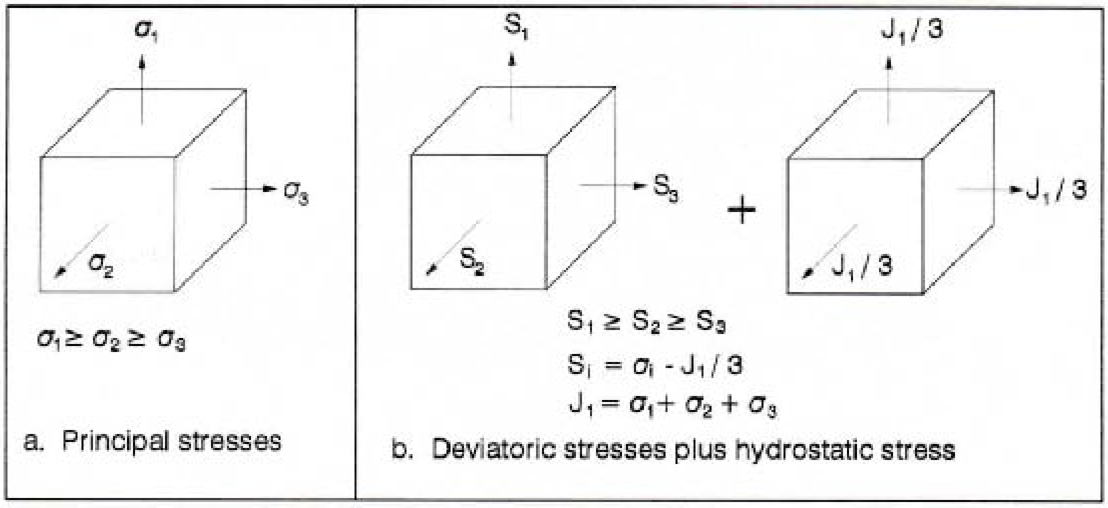
σ_1
σ_3
σ_2
$\sigma_1 \geq \sigma_2 \geq \sigma_3$
a. Principal stresses
S_1
S_3
S_2
+
$J_1/3$
$J_1/3$
$J_1/3$
$S_1 \geq S_2 \geq S_3$
$S_i = \sigma_i - J_1/3$
$J_1 = \sigma_1 + \sigma_2 + \sigma_3$
b. Deviatoric stresses plus hydrostatic stress

Figure 2.1. Principal and deviatoric stresses.

The classical Mohr failure model[1] that is utilized by Civil engineers in soil and rock mechanics was not evaluated in this study because it is not utilized in the design of structures of interest in this study. The Mohr model does allow for the influence of the hydrostatic pressure on failure, but ignores any effect of the intermediate principal stress.

3.0 H2P FAILURE MODEL

The H2P failure model is described in this report section. Beginning with a complex, triaxial stress state with principal stresses σ_1, σ_2, and σ_3, the model in its most general form defines the equivalent stress intensity as

$$\sigma_e = \bar{\sigma} \exp\left[b\left(\frac{J_1}{S_s} + a \right) \right] \tag{3.1}$$

Parameters "a" and "b" are determined such that the model identically fits two failure points in triaxial stress space. The remaining stress parameters are all stress invariant and are defined by the equations:

$$J_1 = \sigma_1 + \sigma_2 + \sigma_3 \tag{3.2}$$

$$\bar{\sigma} = \sqrt{\frac{(\sigma_1 - \sigma_2)^2 + (\sigma_2 - \sigma_3)^2 + (\sigma_3 - \sigma_1)^2}{2}}, \tag{3.3}$$

and

$$S_s = \sqrt{\sigma_1^2 + \sigma_2^2 + \sigma_3^2} \tag{3.4}$$

One can express these same stress parameters in terms of one or more of the classical stress invariants as follows:

$$\bar{\sigma} = \sqrt{3J_2'} \tag{3.5}$$

$$\begin{aligned} S_s &= \sqrt{\frac{6J_2' + J_1^2}{3}} \\ &= \sqrt{J_1^2 - 2J_2} \\ &= \sqrt{3J_2' + J_2} \end{aligned} \tag{3.6}$$

Parameters J_1, J_2, J_2', and $\bar{\sigma}$ have the usual definitions with

J_1 = 1st invariant of the stress tensor

J_2 = 2nd invariant of the stress tensor

J_2' = 2nd invariant of the deviatoric stress tensor

$\bar{\sigma}$ = Mises stress intensity (Mises equivalent stress)

The invariant stress parameters making up the H2P failure model are graphically illustrated in Fig. 3.1. Constraining the model to identically fit the pure tensile failure point (similar to the Mises, Tresca, and Rankine models) results in a value "a" of –1.0. The model then takes the form:

$$\sigma_e = \bar{\sigma} \exp\left[b\left(\frac{J_1}{S_s} - 1 \right) \right] \tag{3.7}$$

Given that σ_0 denotes the pure tensile failure stress, then for any point in triaxial stress space, failure is predicted to occur when:

$$\sigma_e = \sigma_0 \tag{3.8}$$

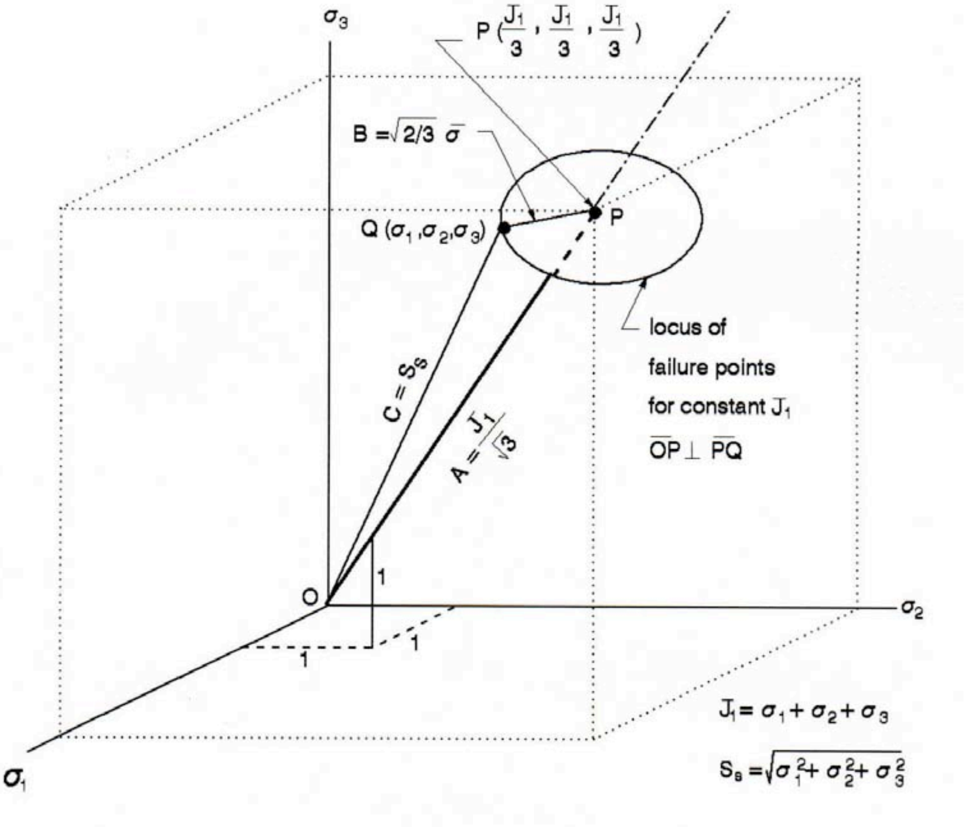

σ_3
$P\left(\frac{J_1}{3}, \frac{J_1}{3}, \frac{J_1}{3}\right)$
$B = \sqrt{2/3}\ \bar{\sigma}$
$Q(\sigma_1, \sigma_2, \sigma_3)$
P
locus of
failure points
for constant J_1
$\overline{OP} \perp \overline{PQ}$
$C = S_s$
$A = \frac{J_1}{\sqrt{3}}$
O
1
1
1
σ_2
σ_1
$J_1 = \sigma_1 + \sigma_2 + \sigma_3$
$S_s = \sqrt{\sigma_1^2 + \sigma_2^2 + \sigma_3^2}$

Figure 3.1. Geometric representation of H2P failure model stress parameters.

Two options exist for determining H2P model parameter "b" from laboratory-type failure data. These are: (1) determine "b" such that the model identically fits a second point in stress/failure space (other than the pure tensile point) and (2) determine "b" using least-squares techniques so that the model provides a best fit to a set of failure tests spanning triaxial stress space. Both methods have been successfully utilized with the model. These two methods are described in the report sections that follow.

3.1 DETERMINING PARAMETER "b" FROM A SECOND FAILURE TEST

Tests of interest for determining "b" from a second point in triaxial stress/failure space include: (1) tests that can easily be conducted in the laboratory and (2) tests that result in a value of "b" that will provide good predictability of failure at other points throughout the triaxial stress space. Two tests meeting criterion 1 are the pure compression test and the pure torsion test. Using the average of several identical compression or torsion tests is more appropriate than using only one test to define "b." Meeting criterion 2 requires assessments of the model using different materials and a range of triaxial stress states. The assessments in this report represent a first step toward meeting these two criteria.

3.1.1 Determining Parameter "b" from a Pure Compression Test

Defining σ_{0c} as the failure stress in a pure compression test, where $\sigma_{0c} \leq 0$, then for a cylindrical specimen loaded by an axial compression stress, the principal stresses at failure are determined by the equations:

$$\sigma_1 = \sigma_2 = 0 \tag{3.9}$$

and

$$\sigma_3 = \sigma_{0c} = -|\sigma_{0c}|. \tag{3.10}$$

At failure the relevant stress parameters for the H2P failure model (Eqs. 3.2 – 3.4) become:

$$J_1 = -|\sigma_{\mu}|, \tag{3.11}$$

$$S_S = |\sigma_{\mu}|, \tag{3.12}$$

and

$$\Pi = |\sigma_{\mu}|. \tag{3.13}$$

Failure at any point in stress space is then defined by

$$\sigma_e = \sigma_0 \tag{3.14}$$

Inserting Eq. 3.7 with the relevant stress parameters (Eqs. 3.11 – 3.13) into Eq. 3.14 leads to the following equation defining parameter "b" based on a single compression failure test (or the average of a set of several duplicate compression tests):

$$b = \frac{1}{2}\mathrm{Ln}\left(\frac{|\sigma_{0c}|}{\sigma_c}\right) \tag{3.15}$$

The H2P failure model based on identically fitting the pure tension and pure compression failure points thus becomes:

$$\boxed{\sigma_e = \bar{\sigma}\exp\left[\frac{1}{2}\,\mathrm{Ln}\left(\frac{|\sigma_{0c}|}{\sigma_0}\right)\left(\frac{J_1}{S_s}-1\right)\right]} \tag{3.16}$$

3.1.2 Determining Parameter "b" from a Pure Torsion Test

With τ_0 defined as the torsional failure stress in a cylindrical specimen under a pure torsion load, principal stresses are determined by the equations:

$$\sigma_1 = \tau_0, \tag{3.17}$$

$$\sigma_2 = 0, \tag{3.18}$$

and

$$\sigma_3 = -\tau_0, \tag{3.19}$$

At failure, the relevant H2P model stress parameters become:

$$J_1 = 0\ , \tag{3.20}$$

$$S_s = \tau_0\sqrt{2}, \tag{3.21}$$

$$\bar{\sigma} = \tau_0\sqrt{3}. \tag{3.22}$$

Failure is predicted to occur when σ_e equals σ_0. Incorporating the relevant stress parameters into Eq. 3.7 and equating to tensile strength, σ_0 , parameter "b," based on a pure torsion failure test (or on the average of a set of duplicate torsion tests), becomes:

$$b = \mathrm{Ln}\left(\frac{\tau_0\sqrt{3}}{\sigma_0}\right) \tag{3.23}$$

The H2P failure model, based on identically fitting the pure tension and pure torsion failure points, thus becomes:

$$\boxed{\sigma_e = \bar{\sigma}\exp\left[\mathrm{Ln}\left(\frac{\tau_0\sqrt{3}}{\sigma_0}\right)\left(\frac{J_1}{S_s}-1\right)\right]} \tag{3.24}$$

3.2 DETERMINING PARAMETER "b" FROM A SET OF M FAILURE TESTS

Parameter "b" in the H2P model can be determined such that the model provides a "best fit" to a set of failure tests encompassing different stress states. For this type of fit, the model does not necessarily identically fit any one of the points other than the pure tension point. Given a set of M failure tests spanning triaxial stress space, one failure equation can be written for each of the M tests (i.e., using Eqs. 3.7 and 3.14). The value of "b" is unknown in each of these equations. For each test the deviation, δ_i , between the predicted value of stress at failure, σ_0, and the observed value of stress at failure, σ_e , becomes

$$\delta_i = \left[\sigma_0 - \sigma_e \exp\left(b\left(\frac{J_1}{S_s} - 1\right)\right)\right] \tag{3.25}$$

The sum of the squared deviations, denoted as SSQ , becomes

$$\mathrm{SSQ} = \sum_{i=1}^{M} \delta_i^2 \tag{3.26}$$

One can now determine the value of parameter "b" that gives the minimum value for SSQ. (This is best done using one's computer.)

Parameter "b" can also be determined somewhat more easily using a second method wherein Eq. 3.25 is linearized by taking its logarithm. Standard linear least-squares techniques can then be used to determining "b." This approach, summarized in Appendix A, was provided by one of the technical reviewers of this paper after completion of the paper. The method is not evaluated in this report.

The H2P failure model is, therefore, expressed by Eq. 3.7. One can determine parameter "b" using any of the three methods outlined: (1) from Eq. 3.15 and a single compression test (or the average of a set of duplicate compression tests); (2) from Eq. 3.23 and a single torsion test (or the average of a set of duplicate torsion tests); or (3) from Eqs. 3.25 and 3.26 and a set of M failure tests spanning triaxial stress/failure space. In subsequent results presented in this report, each of these three methods is successfully utilized for determining "b." While the available triaxial failure data are insufficient to make a definite conclusion as to the best method, all three methods provide improved predictions relative to the classical models of Mises, Tresca, and Rankine. For the assessments based on time-independent failure data, the compression test provides the simplest and most accurate basis for determining parameter "b," as will be shown subsequently.

3.3 MODEL FAILURE SURFACES

One means for visually describing the H2P failure model is to compare the two-dimensional (2-D) failure contour and the three-dimensional failure surface with the analogous contours and surfaces of the classical failure models. These comparisons are made in this report section. Failure contours and surfaces are defined as the contour or surface of constant equivalent stress, $\square_e = \square_0$, where $\square_0$ is the material tensile strength.

Figure 3.2 compares a typical two-dimensional contour for the H2P model with the analogous contours for the classical models. The H2P model contour is plotted for a parameter "b" value of 0.24 (ratio of compression to tensile strength of 1.62). Note that the H2P model (with $b > 0$) predicts that higher compressive stress states are required to produce failure as compared to the same tensile stress state. For parameter "b" less than zero, the H2P model predicts just the opposite requiring higher tensile stresses to produce failure. Because the compressive strength in most materials is higher than the tensile strength, most materials will have a value of "b" greater than zero. For the case of "b" equal to 0.0, the H2P model reduces to the classical Mises model. The classical failure models, being single-parameter models, are unable to capture this important characteristic material behavior, making it difficult for designers to take full advantage of both the compressive and tensile strengths of a material when these strengths differ.

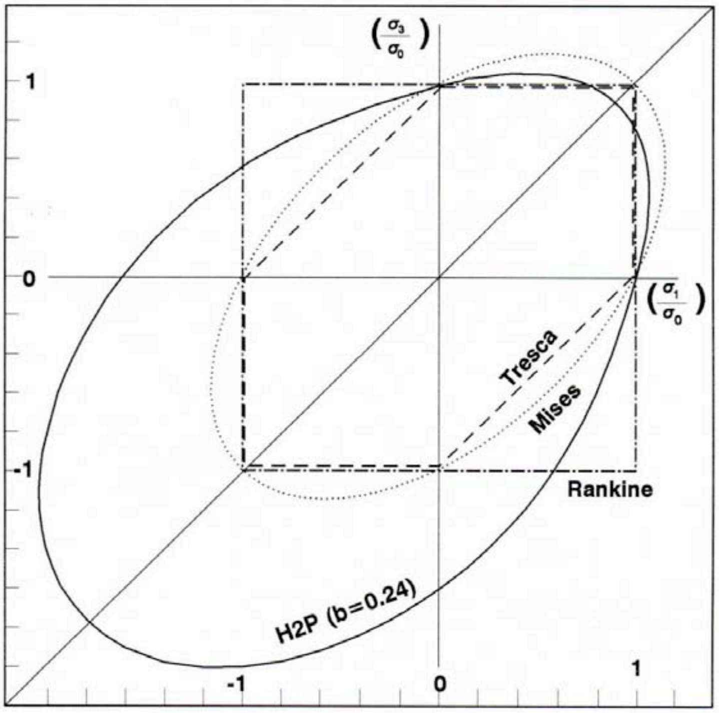

Figure 3.2. Comparison of 2-D failure contours.

Figure 3.3 shows a typical three-dimensional failure surface for the H2P model for a ratio of compressive-to-tensile strength of 1.75 ($b = 0.28$). The bottle-shaped surface extends to ± along the (1,1,1) axis in both the positive ($J_1 > 0$) and the negative ($J_1 < 0$) directions. The analogous surfaces for the Mises and Tresca models are shown in Fig. 3.4 and also extend to ± along the (1,1,1) direction. The ability of the H2P model to capture differences in failure under tensile versus compressive stress states is clearly indicated by the bottle-shaped failure surface, whereas the prismatic shapes of the Mises and Tresca models indicate their inability to capture this difference. The three-dimensional failure surface for the Rankine model is shown in Fig. 3.5. By limiting maximum principal stress, σ_1 , to the tensile strength, σ_0 , and limiting minimum principal stress, σ_3, to the compressive strength, σ_{0c} , one can take advantage of both the tensile and compressive strengths of a material using two equations. However, where triaxial stresses are involved, the Rankine model cannot account for the effect of the hydrostatic pressure (i.e., for $J_1 / 3$) nor for the effect of the intermediate principal stress, σ_2 .

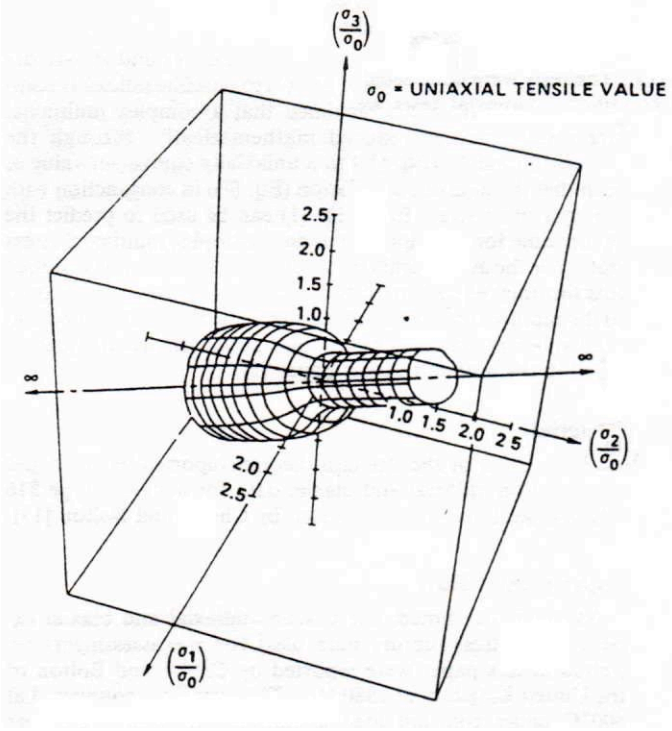
$\left(\frac{\sigma_3}{\sigma_0}\right)$
σ_0 = UNIAXIAL TENSILE VALUE
2.5
2.0
1.5
1.0
∞
∞
1.0
1.5
2.0
2.5
$\left(\frac{\sigma_2}{\sigma_0}\right)$
2.0
2.5
$\left(\frac{\sigma_1}{\sigma_0}\right)$

Figure 3.3. **H2P model failure surface (ratio of compressive to tensile strength of 1.75 [b = 0.28]).**

While these model surfaces (Tresca, Mises, and H2P) extend to ± ∞ in theory, materials may not have infinite strength under both triaxial compression (i.e., $J_1 = +\infty$) and triaxial tension ($J_1 = +\infty$). It is possible that homogeneous materials may have infinite strength in triaxial compression (i.e., a solid sphere may not fail if submerged to an infinite depth in the ocean). However, one could hypothesize that materials can fail at some level of triaxial tension. At very high levels of triaxial tension, failure may occur by separation of atoms at the atomic level. One might, therefore, hypothesize that the bottle-shaped failure surface in Fig. 3.3 has a "cap" at some level of triaxial tension. The author is not aware of any theory or data that might determine such a cap. One could put an arbitrarily imposed cap on triaxial tension for design purposes.

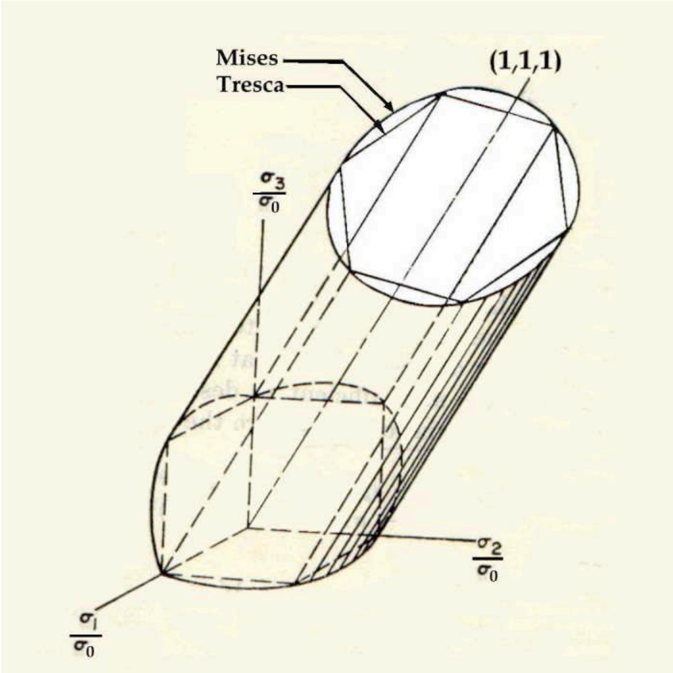
Mises
Tresca
(1,1,1)
$\frac{\sigma_3}{\sigma_0}$
$\frac{\sigma_2}{\sigma_0}$
$\frac{\sigma_1}{\sigma_0}$

Figure 3.4. Mises and Tresca 3-D failure surfaces.

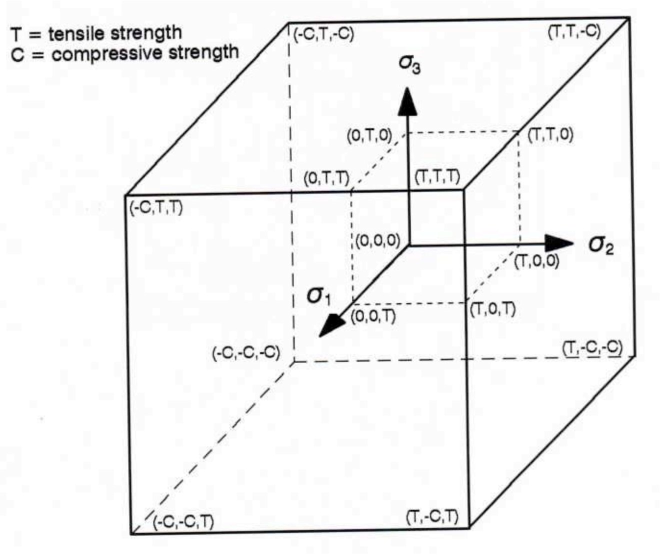
T = tensile strength
C = compressive strength
(-C,T,-C)
(T,T,-C)
σ_3
(0,T,0)
(T,T,0)
(0,T,T)
(T,T,T)
(-C,T,T)
(0,0,0)
σ_2
(T,0,0)
σ_1
(0,0,T)
(T,0,T)
(-C,-C,-C)
(T,-C,-C)
(-C,-C,T)
(T,-C,T)

Figure 3.5. Rankine model 3-D failure surface.

4.0 MODEL / DATA CORRELATIONS

Experimental laboratory data characterizing time-independent and time-dependent failure under different triaxial stress states are utilized to correlate and compare predictions using the H2P failure model with predictions using the classical failure models. Although this type of data is not readily available in the open literature, sufficient data of this type are available such that some model/data correlations can be made. These data and assessments are described in this report section. The failure data, which include tests under both biaxial and triaxial stress states, are summarized below by failure mode and data set.

A. Time-Independent Failure Modes

Data Sets 1 and 2: Tension, compression, and torsion failure tests of cast iron under different hydrostatic pressures (two independent data sets, both using the same cast-iron material).

Data Set 3: Compression failure tests of marble under different hydrostatic pressures.

B. Time-Dependent Failure Modes

Data Sets 4, 5, and 6: Biaxial creep-rupture tests of Types 304 and 316 stainless steels and Inconel 600.

Data Set 7: Uniaxial creep-fatigue tests of two different materials denoted as Material 1 and Material 2.

Failure model/data correlations for these individual data sets follow.

4.1 DATA SET 1 CORRELATIONS—PUGH ET AL. TENSION, COMPRESSION, AND TORSION TESTS OF CAST IRON UNDER HYDROSTATIC PRESSURE

Tests useful for assessment of failure models under triaxial stress states were conducted by Pugh and Green and by Crossland and Dearden. These data were reported by Pugh in 1965.[6] Pugh and Green investigated the effect of hydrostatic pressure on the fracture stress of several materials, including cast iron, at room temperature by testing cylindrical specimens under combined axial tension and hydrostatic pressure. Pugh compared the results to those of Crossland and Dearden,[6] who had conducted similar tests of the same cast-iron material but under (1) combined axial compression and hydrostatic pressure. and (2) combined torsion and hydrostatic pressure. In order to use these results in the current investigation, Pugh's plot of these data must be scaled to develop a numerical data set from which to work. These results and their development and use in assessment of the H2P failure model as well as the classical models of Mises, Tresca, and Rankine are summarized in this report section. The results cover scaling of Pugh's plot, converting the resulting plot parameters into specimen stress parameters, determining material strength values, determining a numerical value for parameter "b" in the H2P model, predicting the stress at fracture based on the H2P model with similar predictions based on the classical models, and finally, comparing these predicted fracture stresses to the experimentally observed stresses at fracture.

4.1.1 Scaling Data Set 1

Pugh[6] reported the previously noted fracture data in the form of plots of "stress at fracture" versus "volumetric compressive stress." This makes it necessary to scale the plot in order to develop a numerical data set from which to work. Although it is preferable not to scale plots, minor differences between scaled values and the actual test results should not significantly alter the results and conclusions for the current assessments.

Pugh plotted maximum principal stress, σ_1, versus volumetric compressive stress which he defined as $-J_1/3$. Scaled values from Pugh's plot are summarized in Table 4.1 and are plotted in Fig. 4.1. In converting these values into the applied loadings, the following nomenclature is utilized:

Z	=	applied tensile or compressive stress (force/area with $Z > 0$ for tension and $Z < 0$ for compression)
W	=	applied torsion stress
P	=	applied hydrostatic pressure
$\sigma_1, \sigma_2, \sigma_3$	=	principal stresses with $\sigma_1 \geq \sigma_2 \geq \sigma_3$
J_1	=	$\sigma_1 + \sigma_2 + \sigma_3$ = 1st invariant of the stress tensor
σ_{cv}	=	$-J_1 / 3$ = volumetric compressive stress
(c,d)	=	scaled values from Pugh's plot (i.e., numerical values in Table 4.1 for $[\sigma_{cv}, \sigma_1]$ for an individual test point)

Conversion of Pugh's plot parameters into the applied specimen loadings Z, W, and P is required in order to compute specimen principal stresses. This is done as follows for each of the applied loading conditions.

Pure Tensile Stress under Hydrostatic Pressure: For a pure tensile stress, Z, applied to a cylindrical specimen under hydrostatic pressure, P, the volumetric compressive stress, and the maximum principal stress are determined by the equations:

$$\sigma_{cv} = \frac{-J_1}{3} = -P - \frac{Z}{3} = c \qquad (4.1)$$

and

$$\square_1 \quad = Z + P = d \qquad (4.2)$$

where "c" and "d" are the scaled values from Table 4.1. The applied stress loadings, Z and P, are determined by solving these two equations simultaneously, giving:

$$P \quad = \frac{\square(3c + d)}{2} \qquad (4.3)$$

and

$$Z \quad = \frac{(3c + d)}{2} \qquad (4.4)$$

where $Z > 0$.

Table 4.1. Data Set 1: scaled data.

Test No.	"c" Volumetric Compressive Stress ($\square_{cv}$) (ksi)	(MPa)	"d" Maximum Principal Stress (ksi)	(MPa)
A. Pure Torsion under Hydrostatic Pressure				
1	0.00	0.0	30.60	211.0
2	7.92	54.6	26.67	183.9
3	16.09	110.9	22.47	154.9
4	32.17	221.8	13.28	91.6
5	47.98	330.8	-0.89	-6.1
6	60.00	413.7	-10.60	-73.1
7	69.99	482.6	-19.27	-132.9
B. Pure Tension under Hydrostatic Pressure				
8	-8.89	-61.3	26.67	183.9
9	-1.04	-7.2	22.20	153.1
10	4.89	33.7	24.30	167.5
11	10.69	73.7	27.72	191.1
12	22.42	154.6	12.23	84.3
13	30.45	210.0	8.82	60.8
14	39.02	269.0	2.78	19.2
15	47.72	329.0	-3.25	-22.4
16	61.03	420.8	-23.73	-163.6
17	66.69	459.8	-25.56	-176.2
18	74.47	513.5	-4.04	-27.9
19	74.99	517.1	-25.56	-176.2
20	77.10	531.6	-31.34	-216.1
21	81.98	565.3	-6.40	-44.1
22	84.22	580.7	-32.39	-223.3
C. Pure Compression				
23	28.08	193.6	0.00	0.00
24	30.00	206.9	0.00	0.00

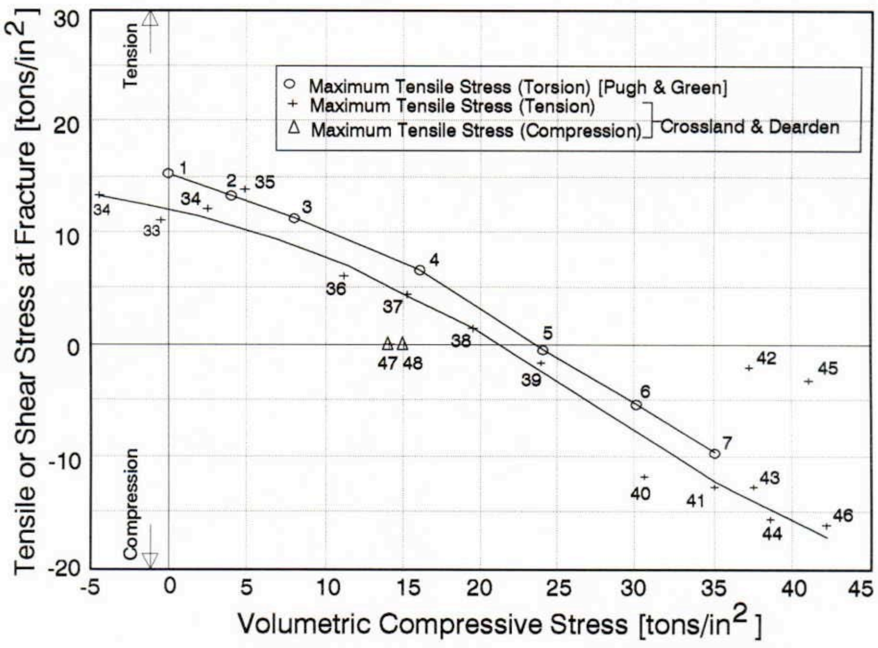

Figure 4.1. **Tensile or shear stress at fracture versus volumetric compressive stress (Source: Pugh^{6})**

Pure Compressive Stress under Hydrostatic Pressure: For a pure compression stress, Z, applied to a cylindrical specimen under a hydrostatic pressure, P, the volumetric stress, and maximum principal stress are determined by the equations:

$$\square_{cv} = \frac{\square J_1}{3} = \frac{\square 3P \square Z}{3} = c \tag{4.5}$$

and

$$\square_1 = +P = d \tag{4.6}$$

Solving these two equations simultaneously for P and Z gives:

$$P = +d \tag{4.7}$$

and

$$Z = -3(c + d) \tag{4.8}$$

where $Z < 0$.

Pure Torsion under Hydrostatic Pressure: For a pure torsion stress, W, applied to a cylindrical specimen under a hydrostatic pressure, P, volumetric stress and maximum principal stress are determined by the equations:

$$\square_{cv} = \frac{\square J_1}{3} = \square P = c \qquad (4.9)$$

and

$$\square_1 = W + P = d \qquad (4.10)$$

Solving these two equations gives the applied loadings, P and W with:

$$P = -c \qquad (4.11)$$

and

$$W = c + d \qquad (4.12)$$

Equations 4.1 – 4.12 provide the basis for converting the scaled values in Table 4.1 into the applied loadings Z, W, and P summarized in Table 4.2.

With the applied specimen loads determined, specimen principal stresses and stress parameters required by the H2P and classical failure models are determined from these values.

4.1.2 Principal Stresses and Stress Parameters

Equations for computing specimen stress parameters are developed from the applied loadings in Table 4.2 for each of the three loading conditions. These equations are summarized in Table 4.3 and, in conjunction with the applied loadings in Table 4.2, are utilized to determine the numerical values for the principal stresses and stress parameters for each of the tests in Data Set 1. The resulting values are summarized in Table 4.4.

4.1.3 Material Strength Properties

Strengths of the cast-iron material in Data Set 1 are determined from the data in Table 4.4, Test 1 (pure torsion), Test 8 (pure tension), and the average of Tests 23 and 24 (pure compression), all conducted under zero hydrostatic pressure. The resulting strengths are:

$$\square_0 = 26.67 \text{ ksi } (183.9 \text{ MPa})$$

$$\square_{0c} = -87.12 \text{ ksi } (-600.7 \text{ MPa}) \qquad (4.13)$$

$$\square_0 = 30.60 \text{ ksi } (211.0 \text{ MPa})$$

Table 4.2. Data Set 1: applied stress loadings at fracture.

Test No.	Stress Fractue (Z or W)		Hydrostatic Pressure (P)	
	(ksi)	(MPa)	(ksi)	(MPa)
A. Pure Torsion under Hydrostatic Pressure				
1	30.60	211.0	0.00	0.00
2	34.59	183.9	-7.92	-54.6
3	38.56	154.9	-16.09	-110.9
4	45.45	91.6	-32.17	-221.8
5	47.09	-6.1	-47.98	-330.8
6	49.20	-73.1	-60.00	-413.7
7	50.72	-132.9	- 69.99	-482.6
B. Pure Tension under Hydrostatic Pressure				
8	26.67	183.9	0.00	0.00
9	31.75	153.1	-9.54	-65.8
10	43.79	167.5	-19.49	-134.4
11	57.61	191.1	-29.89	-206.1
12	51.97	84.3	-39.74	-274.0
13	58.91	60.8	-50.09	-345.4
14	62.70	19.2	-59.92	-413.1
15	66.69	-22.4	-69.95	-482.3
16	55.95	-163.6	-79.67	-549.3
17	61.69	-176.2	-87.25	-601.6
18	105.64	-27.9	-109.68	-756.2
19	74.14	-176.2	-99.71	-687.5
20	68.64	-216.1	-99.98	-689.4
21	113.36	-44.1	-119.76	-825.7
22	77.74	-223.3	-110.13	-759.3
C. Pure Compression				
23	-84.25	580.9	0.00	0.00
24	-90.00	620.6	0.00	0.00

Table 4.3. Equations for principal stresses and stress parameters for three basic loading conditions of cylindrical specimens.*

$\square_1$	$\square_2$	$\square_3$	J_1	⊓	S_s	$\square_{max}$	$\square_{min}$	$\square_{max}$	$\square_v$	$\square_{cv}$
A. Combined Torsion and Hydrostatic Pressure										
W+P	+P	–W+P	3P	$W\sqrt{3}$	$\sqrt{2W^2+3P^2}$	W+P	–W+P	W	P	–P
B. Combined Tension and Hydrostatic Pressure (Z≥0)										
Z+P	P	P	Z+3P	Z	$\sqrt{Z^2+2PZ+3P^2}$	Z+P	P	Z/2	Z/3+P	–Z/3–P
C. Combined Compression and Hydrostatic Pressure (Z≤0)										
P	P	Z+P	Z+3P	|Z□	$\sqrt{Z^2+2PZ+3P^2}$	P	Z+P	$\left\|\frac{Z}{2}\right\|$	Z/3+P	–Z/3–P

*Tensile stresses are always positive, and compressive stresses (including pressure) are always negative.

Table 4.4. Data Set 1: applied loadings and stress parameters.*

Test	P (ksi)	Z (ksi)	W (ksi)	σ_1 (ksi)	σ_2 (ksi)	σ_3 (ksi)	J_1 (ksi)	S_s (ksi)	∏ (ksi)	τ_{max} (ksi)
A. Pure Torsion, W, under Hydrostatic Pressure, P										
1	0.00	0.00	30.60	30.60	0.00	-30.60	0.00	43.28	53.01	30.60
2	- 7.92	0.00	34.59	26.67	-7.92	-42.51	-23.76	50.80	59.91	34.59
3	-16.09	0.00	38.56	22.47	-16.09	-54.65	-48.27	61.24	66.78	38.56
4	-32.17	0.00	45.45	13.28	-32.17	-77.61	-96.50	85.06	78.72	45.45
5	-47.98	0.00	47.09	-0.89	-47.98	-95.07	-143.94	106.49	81.56	47.09
6	-60.00	0.00	49.40	-10.60	-60.00	-109.40	-180.00	125.22	85.56	49.40
7	-69.99	0.00	50.72	-19.27	-69.99	-120.71	-209.96	140.85	87.85	50.72
B. Pure Tension, Z, under Hydrostatic Pressure, P										
8	0.00	26.67	0.00	26.67	0.00	0.00	26.67	26.67	26.67	13.33
9	-9.54	31.75	0.00	22.20	-9.54	-9.54	3.12	25.98	31.75	15.87
10	-19.49	43.79	0.00	24.30	-19.49	-19.49	-14.67	36.75	43.79	21.90
11	-29.89	57.61	0.00	27.72	-29.89	-28.89	-32.06	50.55	57.61	28.81
12	-39.74	51.97	0.00	12.23	-39.74	-39.74	-67.25	57.52	51.97	25.99
13	-50.09	58.91	0.00	8.82	-50.09	-50.09	-91.36	71.39	58.91	29.48
14	-59.92	62.70	0.00	2.78	-59.92	-59.92	-117.08	84.79	62.70	31.35
15	-69.95	66.69	0.00	-3.25	-69.95	-69.95	-143.15	98.97	66.69	33.35
16	-79.67	55.95	0.00	-23.73	-79.67	-79.67	-143.08	115.15	55.95	27.97
17	- 87.25	61.69	0.00	-25.56	-87.25	-87.25	-200.07	126.02	61.69	30.85
18	-109.68	105.84	0.00	-4.04	-109.68	-109.68	-223.40	155.16	105.64	52.82
19	- 99.71	74.14	0.00	-25.56	-99.71	-99.71	-224.98	143.31	74.14	37.09
20	-99.98	68.64	0.00	-31.34	-99.98	-99.98	-231.30	144.83	68.64	34.32
21	-119.76	113.36	0.00	-6.40	-119.76	-119.76	-245.93	169.49	113.36	56.68
22	-110.13	77.74	0.00	-32.39	-110.13	-110.13	-252.65	159.08	77.74	38.87
C. Pure Compression, Z, under Hydrostatic Pressure, P										
23	0.00	-84.25	0.00	0.00	0.00	-84.25	-84.25	84.25	84.25	42.13
24	0.00	-90.00	0.00	0.00	0.00	-90.00	-90.00	90.00	90.00	45.00

* 1 ksi = 6.895 MPa.

4.1.4 H2P Model Parameter "b"

The mathematical expression for the H2P failure model (Eq. 3.7) identically fits the uniaxial tensile failure point and also incorporates model parameter "b" that can be determined such that the model fits another arbitrary point in triaxial stress/failure space. Material strengths for Data Set 1 (Eqs. 4.13) provide a basis for determining parameter "b" using either the results of a pure torsion failure test at zero hydrostatic pressure or a pure compression failure test at zero hydrostatic pressure. It is then possible to determine which of these two test types results in the better correlation of the total data set in Table 4.4.

From Eqs. 3.15 and 3.23 and the cast-iron material strengths in Eqs. 4.13, the following values are determined for parameter "b":

Basis	Parameter "b"	H2P Failure Model
Compression Test	0.592	Eq. 3.7
Torsion Test	0.687	Eq. 3.7

4.1.5 Data Set 1: Model / Data Correlations

Stress equations from Table 4.3, material strengths from Eq. 4.13, and selected failure models are utilized to predict failure for each of the tests in Data Set 1. The results are compared to the observed failures in this report section.

For each test in Data Set 1, the predicted value of the applied stress loading at fracture is determined by equating the equivalent stress intensity, $\square_e$, for each failure model to the material tensile strength, $\square_0$. Equivalent stress intensities were previously defined by Eqs. 2.4 (Tresca), 2.5 (Mises), 2.6 (Rankine), and 3.7 (H2P). These predictions are not described in detail; however, as an example, consider the case of pure torsion under hydrostatic pressure with failure predicted using the Mises model. Expressions for the principal stresses for this case were previously summarized in Table 4.3. Equating the expression for $\sqcap$ from Table 4.3 for combined torsion and hydrostatic pressure to the tensile strength, $\square_0$, results in a predicted torsion stress at fracture of

$$W = \frac{\square_0}{\sqrt{3}} \tag{4.14}$$

Predicting the applied stress at fracture for pure tension and pure torsion under hydrostatic pressure using the Mises, Tresca, and Rankine models for each of the three loading conditions is done in an analogous manner. These predictions result in simple, closed-form equations that can be solved easily for tensile stress, Z, or torsion stress, W. The H2P model requires a bit more work as the resulting equation cannot be solved directly for Z or W. It is necessary to solve the equation numerically. For the case of pure torsion under pressure, when the expression in the H2P model for equivalent stress (Eq. 3.7) is equated to the material tensile strength, σ_0 , the resulting equation for predicting the torsion stress, W, at fracture knowing P and σ_0 is:

$$\sigma_0 - W\sqrt{3}\exp\left[b\left(\frac{3P}{\sqrt{2W^2+3P^2}}-1\right)\right]=0 \qquad (4.15)$$

where the numerical value of the parameter "b" in Eq. 4.15 can be based on choosing either the pure compression or the pure torsion point as the reference. The expressions for "b," for uniaxial compression or pure torsion as the references, are given by Eqs. 3.15 and 3.23, respectively. The equations analogous to Eq. 4.15 for tension and compression under hydrostatic pressure are given in Table 4.5. After the calculated value of "b" is entered into the appropriate equation and a value of P is chosen, the value of Z or W can be calculated numerically by using a root solver.

By using the method described, equations for predicting the applied stress necessary to produce fracture based on the Mises, Tresca, Rankine, and H2P models for all tests in Data Set 1 are developed and are summarized in Table 4.5. These equations, in conjunction with the three material strength values (Eqs. 4.13), are used to predict fracture for all Data Set 1 tests. These results are summarized in Table 4.6 and in Figs. 4.2 through 4.5. Two different values were previously determined for parameter "b" in the H2P model, 0.592 when the model is constrained to identically fit the pure compression point, and 0.687 when it is constrained to identically fit the pure torsion point. Results for b = 0.592 are summarized in Figs. 4.2 and 4.3 with results for b = 0.687 summarized in Figs. 4.4 and 4.5. Three significant conclusions are drawn from these correlations:

1. For this cast-iron material, the classical models of Mises, Tresca, and Rankine provide poor predictions of both the data trend and the numerical values.

2. For this cast-iron material, the H2P model more accurately predicts the fracture trend as well as the numerical value of the stress loads at fracture as compared to the classical models.

3. For these data, H2P model parameter "b," when it is based on the pure compression test, results in more accurate fracture predictions than when based on the pure torsion test.

Table 4.5. **Equations for predicting the applied stress necessary to produce fracture based on the Mises, Tresca, Rankine, and H2P failure models.**

Failure Model	**Fracture Prediction Equation**
A. Pure Torsion under Hydrostatic Pressure	
Mises	$W = \dfrac{\sigma_0}{\sqrt{3}}$
Tresca	$W = \sigma_0/2$
Rankine	$W = \sigma_0 - P$
H2P	$\sigma_0 = W\sqrt{3}\exp\left[b\left(\dfrac{3P}{\sqrt{2W^2+3P^2}} - 1\right)\right]$
(Input σ_0 and P, and then solve numerically for predicted torsion stress, W, at fracture)	
B. Pure Tension under Hydrostatic Pressure	
Mises	$Z = \sigma_0$
Tresca	$Z = \sigma_0$
Rankine	$Z = \sigma_0 - P$
H2P	$\sigma_0 = Z\exp\left[b\left(\dfrac{Z+3P}{\sqrt{Z^2+2PZ+3P^2}} - 1\right)\right]$
(Input σ_0 and P, and then solve numerically for predicted tensile stress, Z, at fracture)	
C. Pure Compression under Hydrostatic Pressure	
Mises	$Z = -\sigma_0$
Tresca	$Z = -\sigma_0$
Rankine	$Z = \sigma_{0c} - P$ where $P<0$ and $\sigma_{0c} < 0$
H2P	$\sigma_0 = \lvert Z\rvert\exp\left[b\left(\dfrac{Z+3P}{\sqrt{Z^2+2PZ+3P^2}} - 1\right)\right]$
(Input σ_0 and P, and then solve numerically for predicted compression stress, Z, at fracture)	

Table 4.6. Data Set 1: comparison of predicted and observed fracture stress.

Test	Observed Stress at Fracture* (ksi)	Predicted Stress (Z or W) at Fracture (ksi)*				
		Mises	Tresca	Rankine	H2P** (b=0.592)	H2P*** (b=0.687)
A. Pure Torsion under Hydrostatic Pressure						
1	30.60	15.40	13.33	26.67	27.83	30.60
2	34.59	15.40	13.33	34.59	36.27	40.41
3	38.56	15.40	13.33	42.76	42.75	48.07
4	45.45	15.40	13.33	58.83	51.78	59.18
5	47.09	15.40	13.33	74.65	57.80	67.05
6	49.20	15.40	13.33	86.67	61.19	71.72
7	50.72	15.40	13.33	96.65	63.45	74.96
B. Pure Tension under Hydrostatic Pressure						
8	26.67	26.67	26.67	26.67	26.67	26.67
9	31.75	26.67	26.67	36.21	39.59	41.23
10	43.79	26.67	26.67	46.15	52.40	55.47
11	57.61	26.67	26.67	56.56	63.88	68.42
12	51.97	26.67	26.67	66.41	73.15	79.16
13	58.91	26.67	26.67	76.76	81.51	89.12
14	62.70	26.67	26.67	86.59	88.33	97.51
15	66.69	26.67	26.67	96.61	94.32	105.15
16	55.95	26.67	26.67	106.34	99.33	111.78
17	61.69	26.67	26.67	113.92	102.75	116.47
18	105.64	26.67	26.67	136.34	110.84	128.21
19	74.14	26.67	26.67	126.37	107.58	123.35
20	68.64	26.67	26.67	126.65	107.68	123.49
21	113.36	26.67	26.67	146.43	113.67	132.60
22	77.74	26.67	26.67	136.80	110.98	128.42
C. Pure Compression						
23	–84.25	-26.67	-26.67	-87.12	-87.12	–105.37
24	–90.00	-26.67	-26.67	-87.12	-87.12	–105.37

* Stress loading (Z for tensile or compressive tests; W for torsion tests).
1 ksi = 6.895 MPa.

** H2P model identically fitting pure compression point.

***H2P model identically fitting pure torsion point.

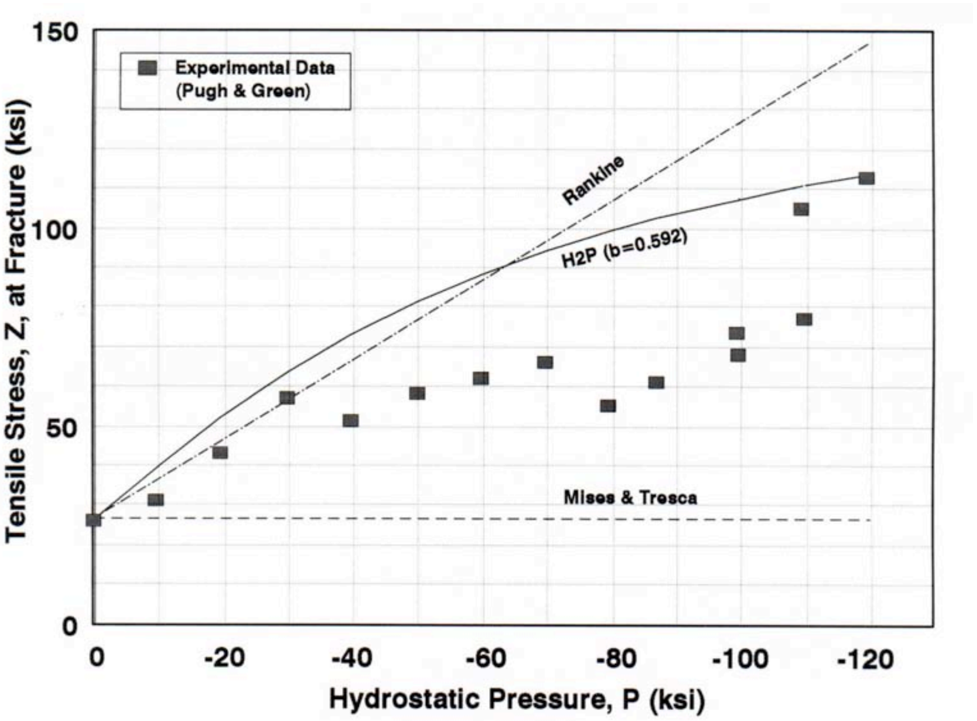

Figure 4.2. Comparison of predicted and observed tensile stress, Z, at fracture for tests of cast iron conducted under combined axial tension, Z, and hydrostatic pressure, P (H2P model parameter "b" determined by pure compression tests).

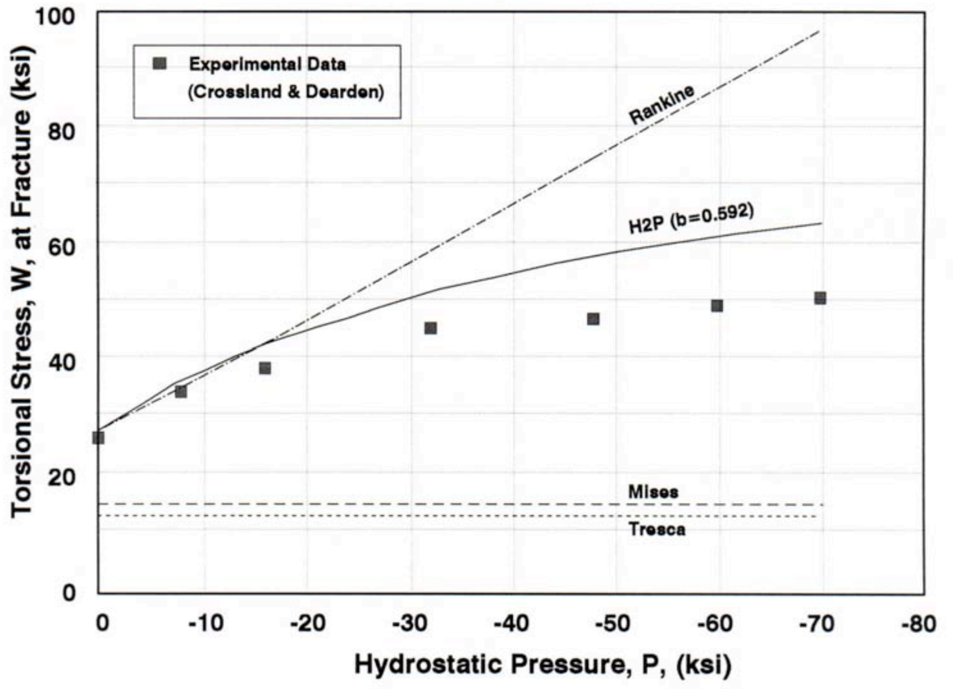

Figure 4.3. Comparison of predicted and observed torsional stress, W, at fracture for tests of cast iron conducted under combined torsion, W, and hydrostatic pressure, P (H2P model parameter "b" determined by pure compression tests).

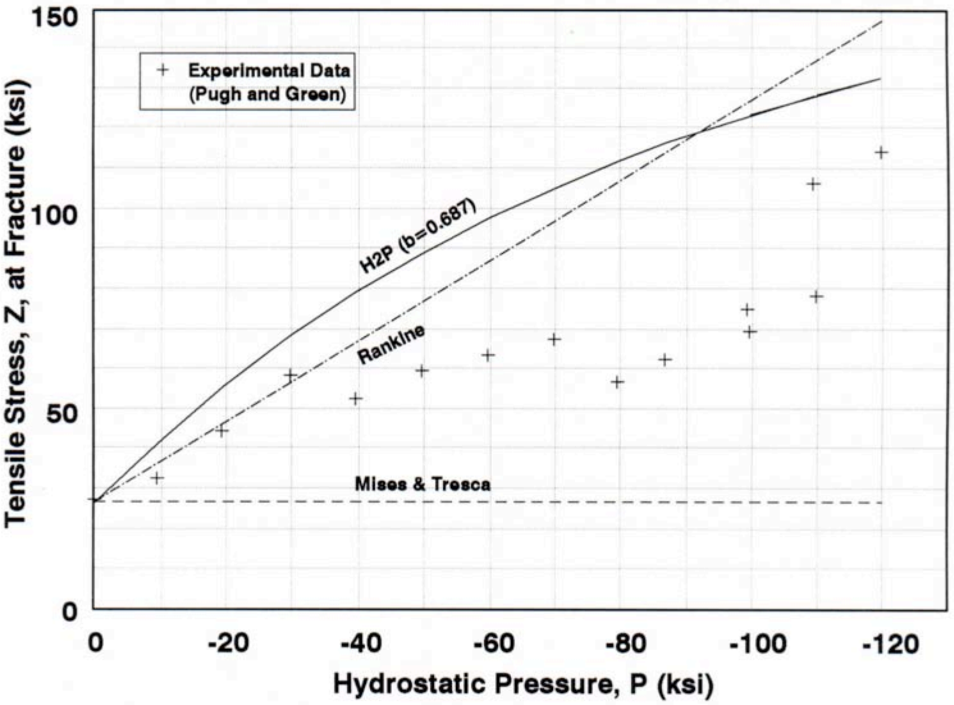

Figure 4.4. Comparison of predicted and observed tensile stress, Z, at fracture for tests of cast iron conducted under combined tension, Z, and hydrostatic pressure, P (H2P model parameter "b" determined by a pure torsion test).

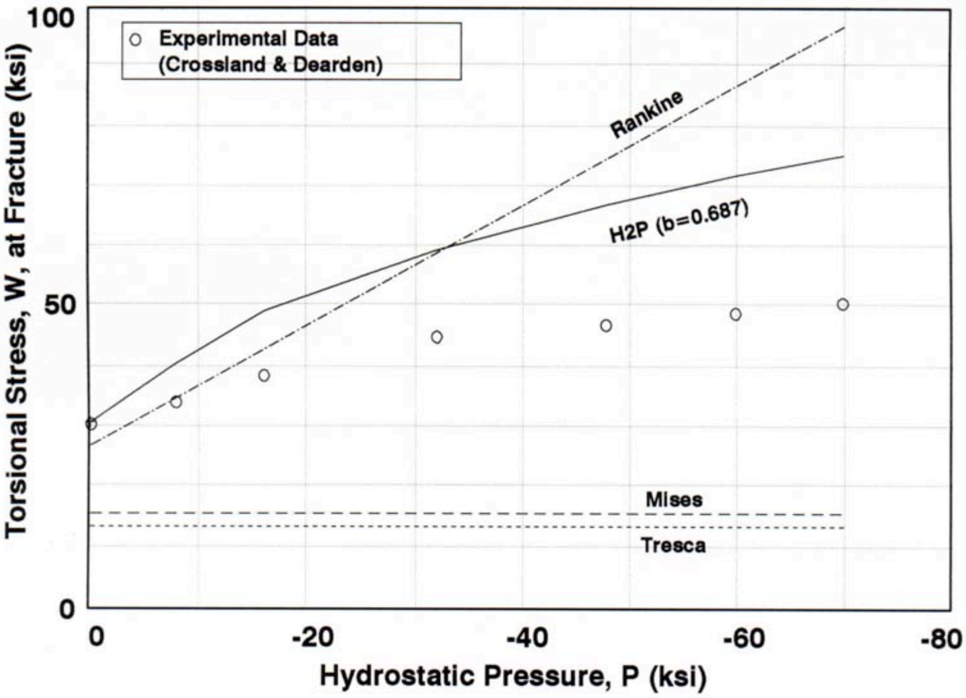

Figure 4.5. Comparison of predicted and observed torsional stress, W, at fracture for tests of cast iron conducted under combined torsion, W, and hydrostatic pressure, P (H2P model parameter "b" determined by a pure torsion test).

4.2 DATA SET 2 CORRELATIONS - CHANDLER AND MAIR TENSION AND COMPRESSION TESTS OF CAST IRON UNDER HYDROSTATIC PRESSURE

In 1967, Chandler[7] reported results of his investigation of cylindrical cast-iron specimens tested to fracture under a triaxial stress state consisting of a pure compression stress plus a hydrostatic pressure. Chandler and Mair,[8] also in 1967, reported similar results for cast-iron specimens tested under pure tension and hydrostatic pressure and under pure compression and hydrostatic pressure. Both sets of results are summarized in Fig. 25.7 of Chandler and Mair[8] in the form of a plot. In order to utilize these data in the current investigation, it is necessary to scale Chandler and Mair's plot and to develop a numerical data set from which to work. This report section, therefore, includes sections covering scaling of Chandler and Mair's plot, converting the resulting values into specimen stress parameters, determining material fracture strength values from the data, determining parameter "b" in the H2P failure model, predicting the applied stress loading at fracture based on the H2P failure model with similar predictions for the classical failure models, and finally comparing the predicted fracture stress/loads to the experimentally observed values.

4.2.1 Scaling Data Set 2

Chandler and Mair[8] reported their results in plotted format, plotting "Maximum Normal Stress" versus "Volumetric Stress." Their plot is scaled in the current investigation to obtain the working data set summarized in Table 4.7 and the curves shown in Fig 4.6. Small differences between these scaled values and the original data should not significantly alter the results or conclusions in the current assessment.

Chandler and Mairs' plot parameters, "maximum normal stress" and "volumetric stress," are interpreted as follows:

Z = applied tensile or applied compressive stress (force/area, with $Z > 0$ for tension and $Z < 0$ for compression)

P = applied hydrostatic pressure

$\sigma_1, \sigma_2, \sigma_3$ = principal stresses ordered $\sigma_1 \geq \sigma_2 \geq \sigma_3$

$J_1 = (\sigma_1 + \sigma_2 + \sigma_3)$ (4.16)

$\sigma_{cv} = -J_1/3$ = volumetric compression stress (4.17)

$\sigma_v = -\sigma_{cv}$ = volumetric stress (4.18)

c(d) = scaled values [i.e., Table 4.7 numerical values for (σ_{cv} , σ_{max}) for an individual test where $\sigma_{max} = Z+P$

These definitions are consistent with the definitions applied in Section 4.1.1, hence Eqs. 4.1 - 4.8 are utilized to convert the scaled values of maximum normal stress and volumetric stress in Table 4.7 into the applied stress loadings, Z and P. These values are also given in Table 4.7. These applied loadings are utilized to compute the specimen stress parameter values needed to utilize selected failure models for predicting fracture for all tests in Data Set 2.

Table 4.7. Data Set 2: Chandler and Mair fracture results for cylindrical, cast-iron specimens tested under combined tension or compression and hydrostatic pressure.

Test No.	Volumetric Stress (σ_{cv}) (ksi)*	Maximum Normal Stress (Z + P) (ksi)	Applied Stress (Z) at Fracture (ksi)	Hydrostatic Pressure (P) (ksi)
A. Pure Tension under Hydrostatic Pressure				
1	-2.418	28.849	-18.051	46.900
2	-4.836	24.485	-19.497	43.982
3	-8.947	29.334	-28.087	57.421
4	-16.442	27.879	-38.603	66.482
5	-16.442	24.485	-36.906	61.392
6	-29.982	22.061	-56.005	78.066
7	-28.774	20.122	-53.222	73.344
8	-45.217	13.819	-74.734	88.553
9	-48.602	5.576	-75.691	81.267
10	-57.307	10.425	-91.172	101.597
11	-64.802	-8.969	-92.719	83.750
12	-75.200	-3.636	-110.982	107.346
13	-77.376	-2.666	-114.731	112.065
14	-91.642	-3.151	-135.888	132.737
15	-94.060	-9.939	-136.121	126.182
16	-98.896	-29.818	-133.435	103.617
17	-104.699	-38.060	-138.019	99.959
B. Pure Compression under Hydrostatic Pressure				
18	-29.016	0.000	-87.048	0.000
19	-52.712	-20.000	-98.137	-20.000
20	-73.024	-40.000	-99.071	-40.000
21	-86.323	-50.000	-108.968	-50.000
22	-117.273	-80.000	-111.819	-80.000
23	-137.826	-100.000	-113.478	-100.000

* 1 ksi = 6.895 MPa.

4.2.2 Principal Stresses and Stress Parameters

Equations for converting applied stress loadings, Z and P, into specimen stresses were previously developed and summarized in Table 4.3. These equations are utilized, in conjunction with the loadings in Table 4.7, to compute relevant stress values for the Chandler and Mair[8] tests. In the interest of brevity, the author has dispensed with including these details in this report because they can easily be determined from the information already given.

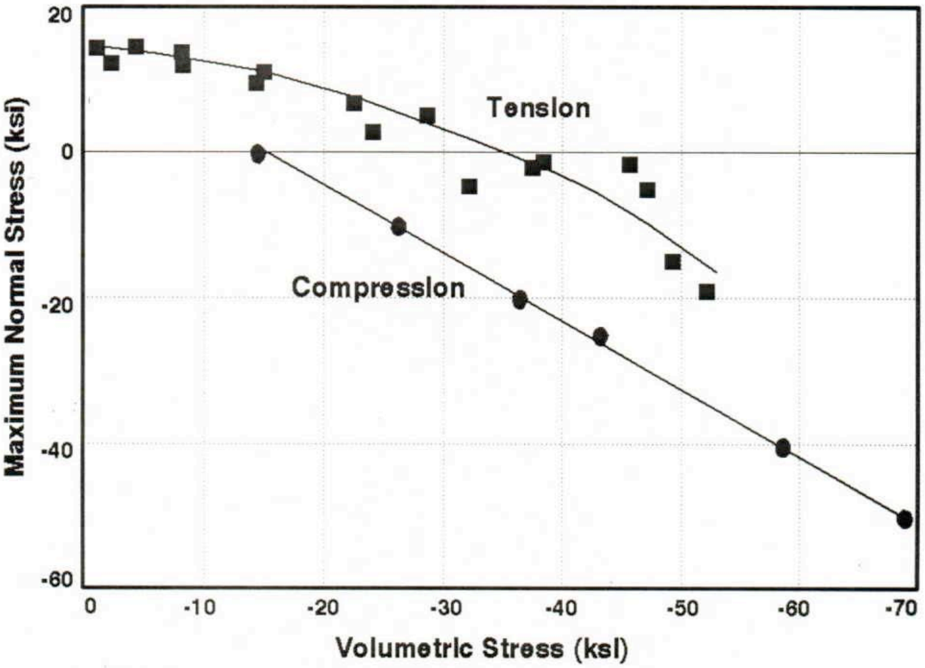

Figure 4.6. **Maximum normal stress versus volumetric stress for cylindrical, cast-iron specimens tested under combined tension or compression and hydrostatic pressure (Sources: Chandler[7], and Chandler and Mair[8]).**

4.2.3 Material Strength Properties

The compressive strength of the cast-iron material utilized in Chandler and Mairs' tests is determined from Test 18 in Table 4.7, as –87.048 ksi (–600.2 MPa). There are no pure tensile tests reported by Chandler and Mair; thus, the tensile strength cannot be directly determined from their data. However, the first five tests in Table 4.7 plot a near straight line. A linear regression fit to these five points is performed and the regression equation extrapolated to zero hydrostatic pressure. This results in a tensile fracture strength of 27.78 ksi (191.5 MPa). The resulting tensile and compressive fracture strengths determined for the cast-iron material are, therefore:

$$\square_{o} = 27.78 \text{ ksi } (191.5 \text{ MPa}) \qquad (4.19)$$

$$\square_{oc} = -87.05 \text{ ksi } (600.2 \text{ MPa})$$

4.2.4 H2P Model Parameter "b"

An equation for determining parameter "b" for the H2P failure model was previously developed (Eq. 3.15) based on the model identically fitting the pure compression failure point at zero hydrostatic pressure. When Eq. 3.15 is utilized in conjunction with the material strengths from Eqs. 4.19, the resulting value for parameter “b” for Chandler and Mair’s cast-iron material becomes:

$$b = 0.5711 \tag{4.20}$$

One now has all the necessary analytical tools for predicting the applied tensile or compression loading, Z, for Chandler and Mair’s tests under hydrostatic pressure, P.

4.2.5 Data Set 2: Model / Data Correlations

Equations for predicting the applied stress loading required to produce fracture under a given hydrostatic pressure were previously developed and were summarized in Table 4.5. These equations are utilized for predicting fracture for all Data Set 2 tests. These results are compared to the observed fracture results in Figs. 4.7 and 4.8 for the tensile and compressive tests, respectively. The classical models of Mises and Tresca each demonstrate poor predictions for both the tensile and compressive tests under hydrostatic pressure. The Rankine model demonstrates somewhat better predictions for the tensile tests under pressure although its linear prediction trend with increasing hydrostatic pressure does not match the data trend. The Rankine model provides poor predictions for the compression tests under hydrostatic pressure, as shown in Fig. 4.8. The H2P model demonstrates excellent predictions for both the tensile and compression tests under hydrostatic pressure.

4.3 DATA SET 3 CORRELATIONS—VON KARMAN TENSION AND COMPRESSION TESTS OF MARBLE UNDER HYDROSTATIC PRESSURE

T. von Karman*in 1911 investigated the effect of hydrostatic pressure on the compressive strength of cylindrical specimens of marble. His results were summarized by Nadai [9] in Fig. 17-1 of his 1950 book entitled *Theory of Flow and Fracture of Solids.* The H2P failure model and the classical models of Mises, Tresca, and Rankine are utilized in the current work to predict the applied stress load at failure for each of von Karman’s tests. The results are then compared to the experimentally observed failure stress values. Nadai published von Karman’s data in the form of a plot of “$(\sigma_1 - \sigma_2)$” versus “Unit Compression.” Nadai, however, utilized a different definition for these parameters than what has been used in this report. In order to utilize von Karman’s data in the current work, it is necessary to scale Nadai’s plot, then convert the data to the nomenclature that has been adopted in this report, thus providing a working data set for the current analyses. This section, therefore, covers scaling of Nadai’s plot, converting the scaled values to the nomenclature adopted in this report and then into the stress parameters needed by specific failure models, determining the material strength properties, determining parameter “b” for the H2P failure model, and finally predicting the applied stress loading for each of von Karman’s tests and comparing these to the observed data.

---

*Forschungsheft 118, and Z. Ver. Deut. Ing., 1911.

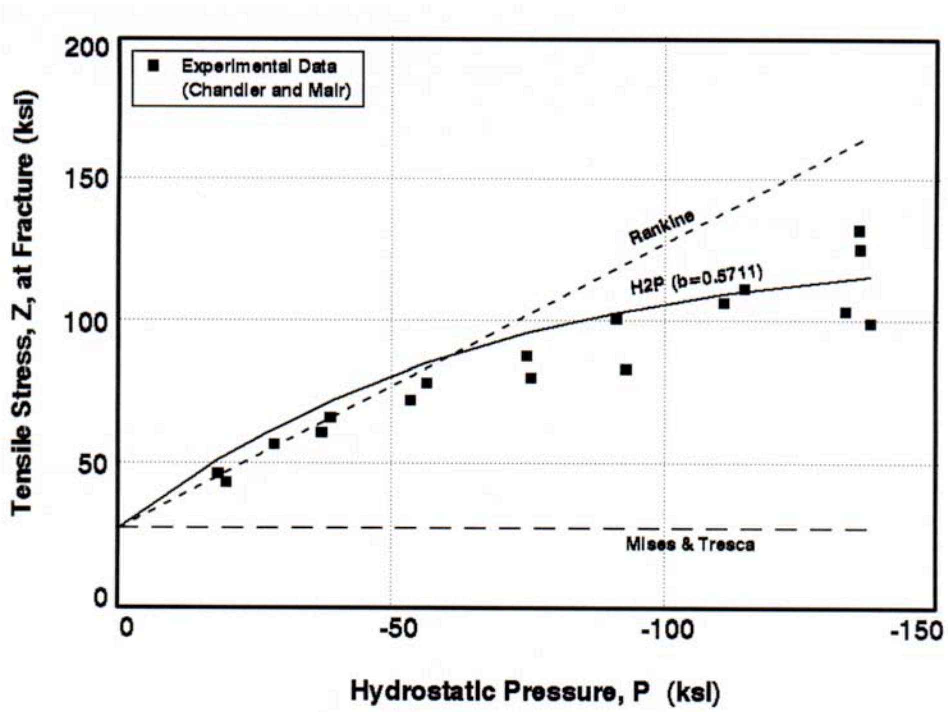

Figure 4.7. Comparison of predicted and observed tensile stress, Z, at fracture for cylindrical, cast-iron specimens tested under combined tension, Z, and hydrostatic pressure, P (H2P model parameter "b" determined by pure compression test).

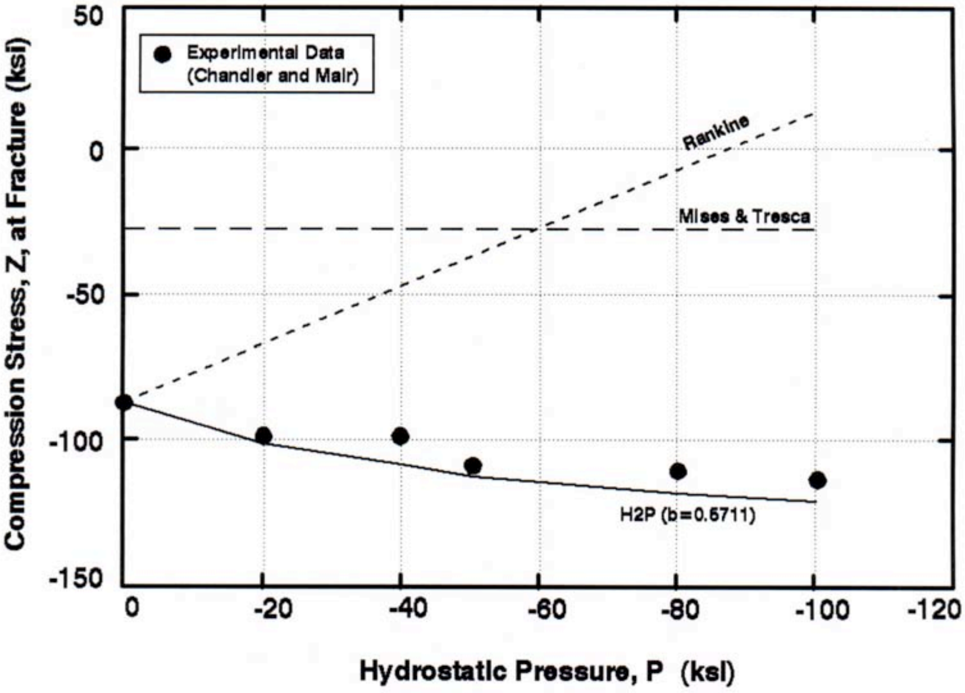

Figure 4.8. Comparison of predicted and observed compressoion stress, Z, at fracture for cylindrical, cast-iron specimens tested under combined compression, Z, and hydrostatic pressure, P (H2P model parameter "b" determined by compression test).

4.3.1 Scaling Data Set 3

Von Karman's data, as published by Nadai[9], are reproduced in Fig. 4.9. The data are plotted as (σ_1 – σ_2) versus Unit Compression (%) where σ_1 , σ_2 , and σ_3 denote the principal stresses and Unit Compression denotes the strain along the cylindrical specimen axis (i.e., along σ_1 direction). When the applied axial stress is defined as Z and the hydrostatic pressure as P, the abscissa and ordinate of Nadai's plot can be described as follows. Principal stresses σ_1 , σ_2 , and σ_3 correspond to the cylindrical coordinates σ_z , σ_r , and σ_θ. In terms of the applied loadings, the principal stresses for the cylindrical specimen in Nadai's nomenclature become:

$$\sigma_1 = \sigma_z = Z+P, \tag{4.21}$$

$$\sigma_2 = \sigma_r = P, \tag{4.22}$$

and

$$\sigma_3 = \sigma_\theta = P \tag{4.23}$$

Nadai's plot axes are then:

abscissa: Unit Compression (%) = $\varepsilon_1 = \varepsilon_z$

ordinate : $(\sigma_1 - \sigma_2) = (\sigma_z - \sigma_r) = Z$

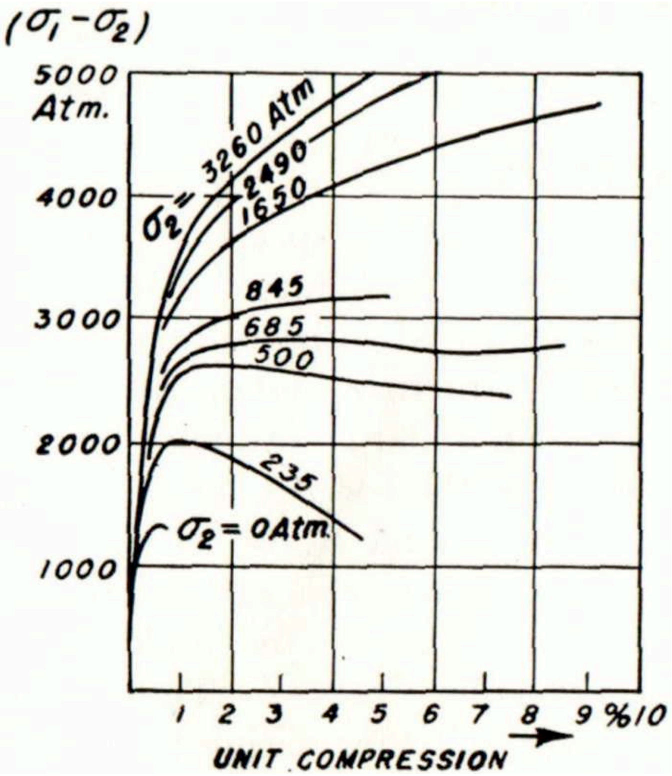

Figure 4.9. T. von Karman failure tests of marble cylinders under combined axial compression and hydrostatic pressure (Source: Nadai[9]).

In order to be consistent with the nomenclature adopted in the current report, the scaled data are converted to the following nomenclature for further use in this report:

σ_1 , σ_2 , σ_3 correspond to the cylindrical coordinates σ_θ , σ_r , σ_z where $\sigma_1 \geq \sigma_2 \geq \sigma_3$.

$$\sigma_1 = \sigma_\theta = P \qquad (4.24)$$

$$\sigma_2 = \sigma_r = P \qquad (4.25)$$

$$\sigma_3 = \sigma_z = Z + P \qquad (4.26)$$

abscissa: Unit Compression (%) = $\varepsilon_3 = \varepsilon_z$

ordinate : $(\sigma_1 - \sigma_3) = (\sigma_\theta - \sigma_z) = -Z$

Nadai's plot, therefore, shows the absolute value of the applied axial stress, Z, versus the axial strain ε_3 (or ε_z) , and Eqs. 4.5 – 4.8, Section 4.1.1, are now valid and are used for scaling Nadai's plot.

In scaling Nadai's plot, it is necessary to define failure in each test. Some of the tests/curves result in fracture of the specimen after it reaches its maximum value and unloading begins. In other tests conducted at higher values of hydrostatic pressure, the curves do not bend over before fracture. In the case of the two curves at the two highest test pressures, the curves terminate when they reach the top of the plot. One is unable to determine if fracture occurs at that point or whether Nadai^9 (or von Karman) omitted the end of the curve. Differences in the curves thus make it difficult to define fracture on a consistent, objective basis. One cannot define failure as the maximum point on each curve or as the end point on each curve with any degree of certainty. This author, therefore, chose to use a 0.45% strain offset method to define failure in each test. The method is the same as that used to determine the 0.2% yield stress in conventional laboratory tensile and compression tests. Several different values of offset were considered. In the end, the choice of 0.45%, which was a subjective choice on the author's part, was easiest to implement and gave some consistency in where the offset modulus line crossed each curve, determining the failure point. The resulting data are summarized in Table 4.8.

4.3.2 Principal Stresses and Stress Parameters

Equations for determining principal stresses and stress parameters needed for predicting failure by the selected failure models were previously developed and summarized in Table 4.3. Details of these calculations are omitted in the interest of brevity as they can easily be reproduced from the information that has been provided.

Table 4.8. **Applied loadings at "failure" for cylindrical specimens of marble tested under combined axial compression, Z, and hydrostatic pressure, P, by T. von Karman (In Nadai[9]).**

Test No.	Applied Loadings at "Failure" (ksi)*	
	Compression Stress,** $Z = \sigma_3 - \sigma_1$	Hydrostatic Pressure (P)
1	–19.62	0.000
2	–29.23	–3.454
3	–35.59	–7.348
4	–37.62	–10.067
5	–39.78	–12.418
6	–45.60	–24.248
7	–48.04	–36.593
8	–50.61	–47.909

* 1 ksi = 6.895 MPa.
** Failure determined by 0.45% strain offset method.

4.3.3 Material Strength Properties and H2P Model Parameter "b"

Von Karman conducted one compression test under zero hydrostatic pressure (Test 1). This result determines the compression strength, σ_{oc} , as –19.62 ksi (–135.3 MPa). There are no tensile tests conducted at zero hydrostatic pressure from which to determine tensile strength, σ_o. One option for estimating the tensile strength from von Karman's data is to correlate the total data set based on the H2P failure model determining the value of model parameter "b" such that it gives the best model fit to von Karman's data (i.e., determine the value of parameter "b" that minimizes the sum of the squared deviations between predicted and observed compression stress, Z, at failure). After determining a value for parameter "b," the tensile strength of the marble material is determined from Eq. 3.15 and the material compressive strength. The method described is utilized to determine the value of "b" and then to estimate the tensile strength of the marble material tested by von Karman. The resulting value of "b" is 1.58 with the tensile strength being 0.832 ksi (5.7 MPa). A tensile strength of this magnitude appears to be a very reasonable value for marble, which is a brittle material with a low tensile and a high compressive strength.

The strength values for marble as utilized in the assessment of von Karman's data are therefore:

$$
\begin{aligned}
\sigma_o &= 0.832 \text{ ksi } (5.7 \text{ MPa}) \\
\sigma_{oc} &= -19.62 \text{ ksi } (-135.3 \text{ MPa})
\end{aligned}
\qquad (4.27)
$$

The corresponding value of parameter "b" for the H2P failure model is:

$$b = 1.58 \tag{4.28}$$

4.3.4 Data Set 3: Model / Data Correlations

Equations for predicting failure by selected failure models given material strengths and applied loadings, Z and P, were developed in Section 4.1, and are summarized in Table 4.5. These equations are utilized for predicting failure for all of the von Karman tests. The results are summarized in Fig. 4.10. For the von Karman marble data, the H2P failure model provides excellent predictions of both the data trend and the failure stresses. The classical models provide poor predictions for these data. This finding is consistent with the findings for the Data Set 2 compression tests of cast iron.

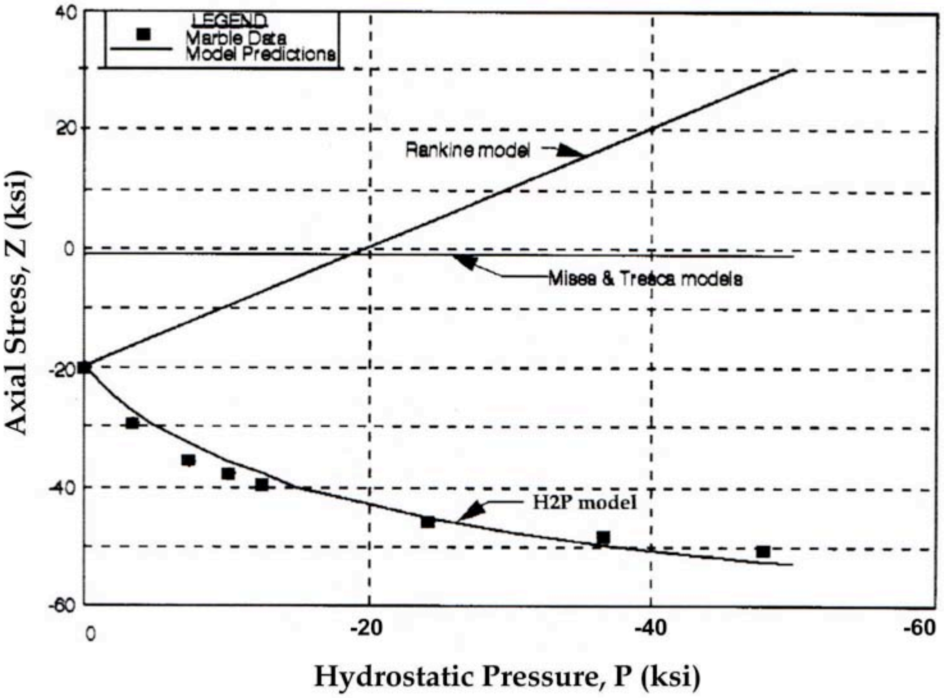

Figure 4.10. Comparison of predicted and observed axial stress, Z, at fracture for marble cylinders tested under combined compression, Z, and hydrostatic pressure, P (H2P model parameter "b" determined by pure compression test).

4.4 DATA SET 4 CORRELATIONS—CHUBB AND BOLTON BIAXIAL CREEP-RUPTURE TESTS OF TYPE 316 STAINLESS STEEL

The H2P failure model was initially developed and applied to improve life predictions in nuclear reactor components operating in the elevated-temperature, creep-rupture region. Correlation of biaxial creep-rupture data for three different alloy steels, Types 304 and 316 stainless steels (SS) and Inconel 600, resulted in 2–3 orders of magnitude reduction in the scatter between predicted and observed lives. Results for one material, Type 316 stainless steel, are summarized in this report section to demonstrate application of the model for predicting creep-rupture and to demonstrate the type of results that have been achieved. The reader is referred to References 2, 4, and 5 for the balance of these results for the three alloy steels noted above. In order to demonstrate the applicability of the H2P failure model for predicting stress rupture, the Type 316 stainless-steel biaxial stress-rupture data and correlations are provided in the current report. The methodology utilized for predicting stress-rupture is summarized, and predicted specimen lives are compared to the observed lives based on the H2P and classical models.

4.4.1 Biaxial Creep-Rupture Data

Chubb and Bolton[10] investigated creep-rupture in Type 316 stainless-steel specimens at 1112°F (600°C) using two specimen types: (1) a solid bar specimen loaded by combined axial tension and torsion; and (2) a tubular specimen loaded with internal pressure and axial tension. Chubb and Bolton's data are summarized in Table 4.9. These data provide the basis for the failure model assessments described in this section.

Table 4.9. Data Set 4: biaxial creep-rupture of annealed Type 316 stainless-steel cylindrical specimens tested at 1112°F (600°C) in air by Chubb and Bolton[10].

Test No.	Biaxial Stress Ratio	σ_x (ksi)*	σ_y (ksi)*	σ_z (ksi)*	T_r (h)	Specimen Loading Mode**
1	2.0	18.389	36.776	–0.450	480	P
2	2.0	16.447	32.891	–0.402	2376	P
3	1.0	27.534	27.434	–0.389	2522	Z+P
4	1.0	23.510	23.510	–0.332	7000	Z+P
5	0.5	31.669	15.835	–0.225	327	Z+P
6	0.5	31.669	15.835	–0.225	1208	Z+P
7	0.0	27.556	0.000	0.000	3141	Z
8	–0.5	25.584	0.000	–12.685	1036	Z+W
9	–0.5	21.337	0.000	–10.587	5839	Z+W
10	–1.0	19.485	0.000	–19.485	2700	W
11	–1.0	19.485	0.000	–19.485	2928	W
12	–1.0	22.492	0.000	–22.492	1121	W
13	–1.0	18.422	0.000	–18.422	4488	W
14	–1.0	18.422	0.000	–18.422	4680	W

* 1 ksi = 6.895 MPa.

**P (internal pressure).
Z (axial tension)
W (torsion).

To use the individual biaxial data in Table 4.9 to objectively assess stress state effects, the effects of material and testing variability are minimized. To do this, an "averaged biaxial data set" is created from the data in Table 4.9. This is accomplished by linearly averaging, in log(stress) versus log(rupture time) space, each subset of the biaxial data having the same stress state (i.e., the same biaxial stress ratio). This reduces the data in Table 4.9 to the six data summarized in Table 4.10 with only one representative average data point for each independent stress state.

Table 4.10. Data Set 4: *averaged* biaxial creep-rupture data of annealed Type 316 stainless-steel cylindrical specimens tested at 1112°F (600°C) in air by Chubb and Bolton[10].

Biaxial Stress Ratio	σ_x (ksi)*	σ_y (ksi)*	σ_z (ksi)*	T_r (h)	Specimen Loading Mode
2.0	17.389	34.777	–0.425	1068	P
1.0	25.443	25.443	–0.360	4202	Z+P
0.5	31.669	15.835	–0.225	629	Z+P
0.0	27.492	0.000	0.000	1958	Z
–0.5	23.365	0.000	–11.561	2460	Z+W
–1.0	19.607	0.000	–19.607	2844	W

* 1 ksi = 6.895 MPa.

4.4.2 Methodology for Predicting Creep-Rupture

Given the stationary stress state, σ_{ij} , and operating temperature, T_1 , for a structural component, two additional elements are required for predicting creep-rupture: (1) a failure model and (2) a baseline uniaxial creep-rupture correlation. The classical failure models and the H2P model are described in Section 2.0 by Eqs. 2.4 – 2.6 and Eq. 3.7, respectively. It is assumed that the baseline uniaxial creep-rupture correlation for a specific temperature, T_1 , is expressed by the normal equation:

$$T_r = g\sigma^h \tag{4.29}$$

where:

T_r = rupture time

σ = uniaxial stress

g, h = material constants

Rupture time under a complex triaxial stress state is then predicted by the equation:

$$T_r = g\sigma_e^h \tag{4.30}$$

4.4.3 Data Set 5: Data / Model Correlations

Results of the assessment of the H2P and the classical failure models based on the data in Table 4.10 are summarized in two forms: (1) a two-dimensional (2-D) biaxial isochronous stress-rupture contour, and (2) a polar plot showing deviations between predicted and observed specimen lives as a function of stress state. The polar plot is a convenient means to show which stress states result in the best and the worst life predictions. Parameter "b" for the H2P failure model (Eq. 3.7) is determined by a least-squares fit of the model to the data in Table 4.10 with the resulting value being 0.1893. It should be noted that "b" for the three materials evaluated to date (Types 304 and 316 stainless steels and Inconel 600) demonstrates a somewhat universal value[4] of about 0.24 for predicting creep-rupture in these alloy steels. The value of 0.1893 was, however, utilized in the current assessments. By comparison, the value of "b" determined from Eq. 3.23 and the tension and torsion tests in Table 4.10 is 0.211.

Biaxial isochronous stress rupture contours (contour based on a constant rupture time, T_r, and a constant value of equivalent stress, σ_e) for the four failure models evaluated are shown in Fig. 4.11. One can see that the H2P model describes the data much better than do the classical models, particularly in the second and fourth quadrants where tension-compression stress states exist.

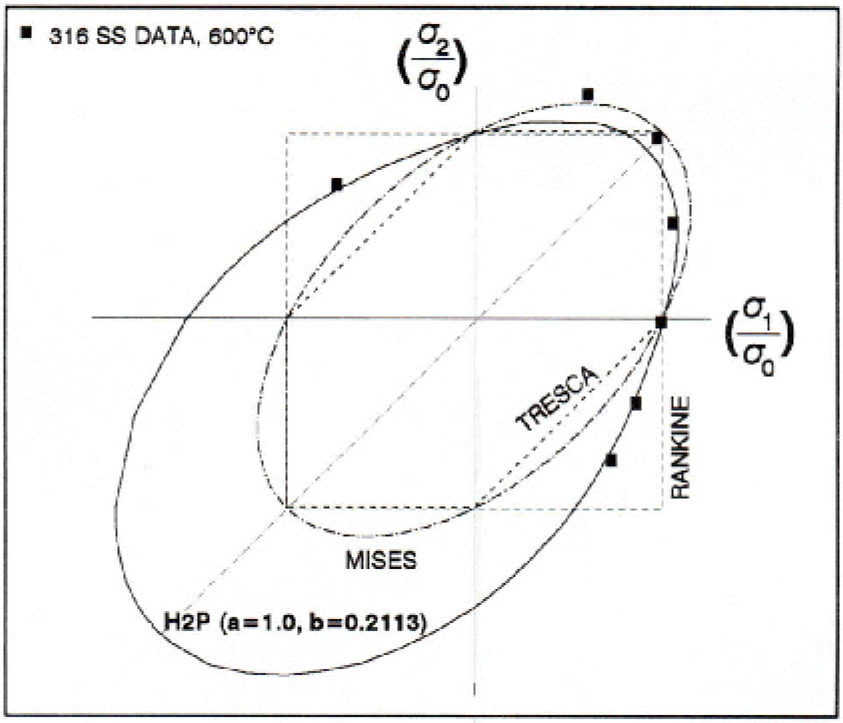

Figure 4.11. Correlation of Type 316 stainless-steel biaxial stress-rupture data with 2-D isochronous stress-rupture contours.

For creep-rupture tests under biaxial stress states, polar plots provide an excellent means for displaying deviations between predicted and observed life as a function of the biaxial stress state. Plots of this type are developed and are shown in Figs. 4.12 through 4.15 for the failure models that were evaluated. In these plots the ratio of predicted-to-observed rupture time is plotted radially in logarithmic scale with the plot axes and angle mapping the principal stress axes in the specimen wall. For each biaxial test, the tangent of the angle, □ , in the polar plot is defined by the biaxial stress ratio for the specific test. If a failure model is perfect (i.e., exactly predicts failure at all stress states) the data will fall around a circle of radius 1.0 [i.e., Log(10^0)]. If a data point falls radially outside this circle, life is over-predicted. Similarly, if a point falls inside this circle, life is under-predicted. A circle labeled as "SM-20" (observed life is 20 times predicted life) is placed on the plot as a base of reference and denotes a safety margin of 20 on life (the approximate ASME CCN47, Appendix T, safety margin).[3] Similarly, a circle labeled OCM-5 (observed life is 1/5 predicted life) is placed on each plot as a second base of reference and denotes an arbitrarily assigned margin of 5 on life indicating the possibility of over-design.

In comparing the polar plot results, the H2P model (Fig. 4.12) provides the best predictions for these data with the greatest deviations occurring for two tension-tension (T-T) stress states. Both the Mises (Fig. 4.13) and the Tresca (Fig. 4.14) models result in highly conservative life predictions for biaxial tension-compression (T-C) stress states. The Rankine model (Fig. 4.15) results in significant life over- predictions under T-C stress states, and for some T-C stress states predictions exceed a safety margin of 20.

The trends observed in the Type 316 stainless-steel biaxial tests and failure model assessments are very similar to those observed for Types 304 stainless steel[2] and Inconel 600.[5] In addition, parameter “b” in the H2P failure model has similar values for these three alloy steels (0.29 for Type 304 SS, 0.19 for Type 316 SS, and 0.25 for Inconel 600). A universal value of 0.24 has been evaluated previously by the author (Refs. 2 and 4), and it provides predictions significantly better than the classical failure models for these three alloy steels. This universal value of “b” is anticipated to result in significantly improved life predictions for other similar alloy steels.

4.5 CREEP-FATIGUE LIFE PREDICTION METHODOLOGY

This report section summarizes a proposed change to the current, linear-damage-based, life-prediction methodology utilized by ASME Code Case N47[3] for design of structures operating at elevated temperature under cyclic creep-fatigue conditions. The current design method incorporates (1) a linear time and cycle fraction damage model; (2) a bilinear creep-fatigue damage interaction diagram that limits total damage; and (3) the Mises equivalent stress model to accommodate triaxial stresses. The proposed change appears to have the potential to improve the accuracy of life predictions, particularly where creep damage occurs under compressive stress states.

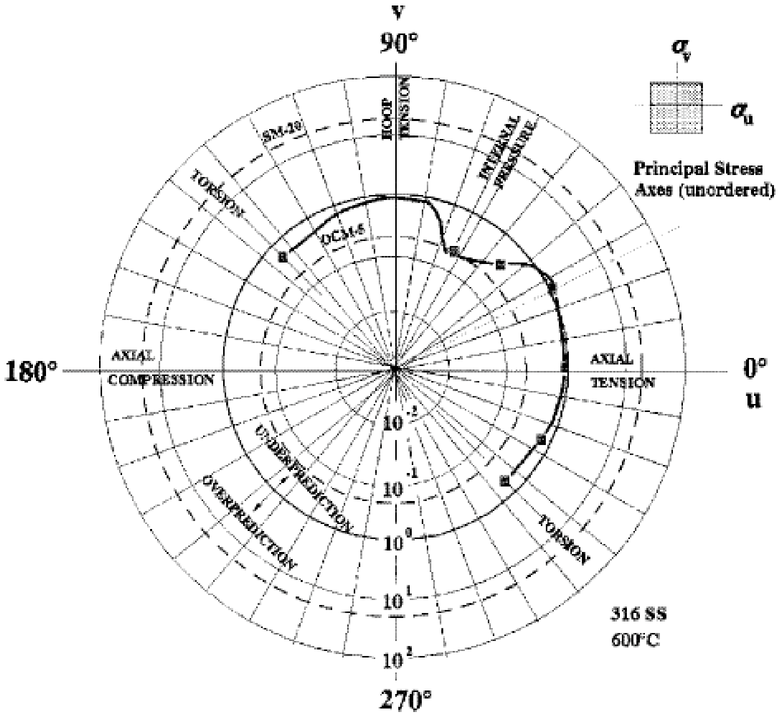

Figure 4.12. Correlation of the ratio of predicted-to-observed life with stress state based on the H2P failure model.

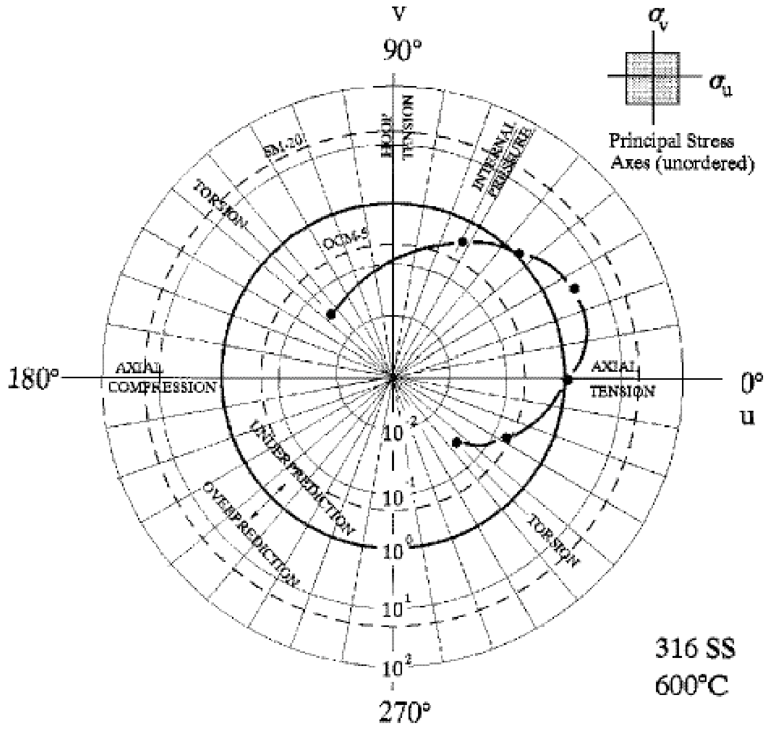

Figure 4.13. Correlation of the ratio of predicted-to-observed life with stress state based on the Mises failure model.

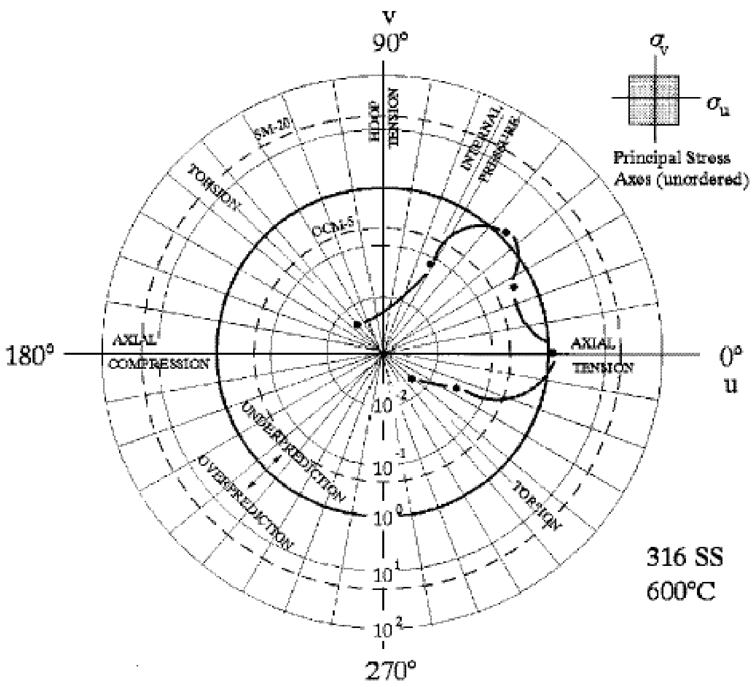

Figure 4.14. Correlation of the ratio of predicted-to-observed life with stress state based on theTresca failure model.

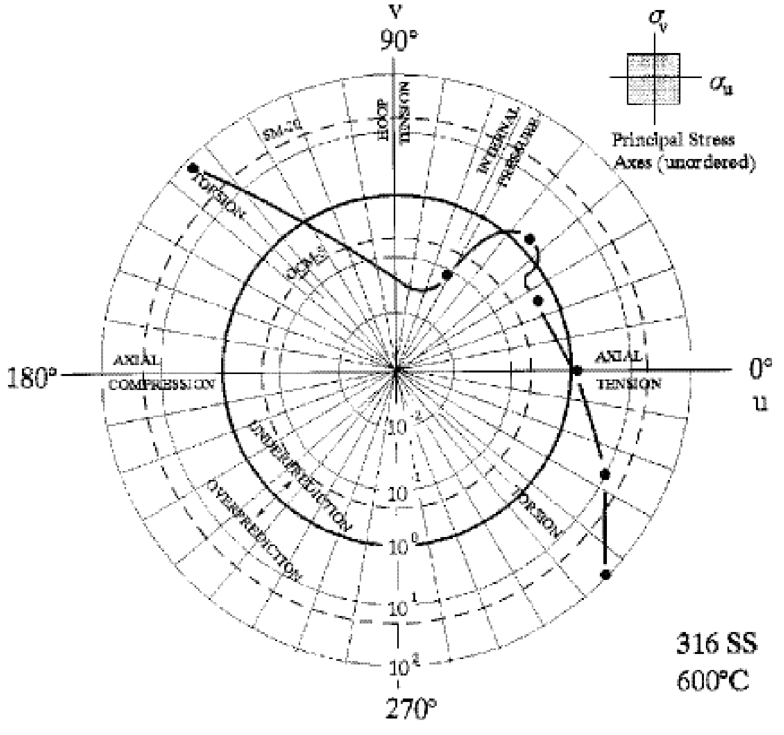

Figure 4.15. Correlation of the ratio of predicted-to-observed life with stress state based on the Rankine failure model.

The proposed change to the existing design methodology incorporates the conventional linear damage model as well as the bilinear creep-fatigue interaction diagram, but it replaces the conventional Mises equivalent stress model with the H2P equivalent stress model. As previously noted, the H2P model has been shown to significantly improve creep-rupture life predictions and has been incorporated into the ASME Code[3] for design of structures operating under creep-rupture conditions. The author believes the model may also have the potential to significantly improve creep-fatigue life predictions, particularly where stress relaxation occurs under compressive stresses. The life of materials tested under creep-fatigue conditions can differ considerably for stress-strain cycles with a tensile versus a compressive strain hold period (i.e., creep damage accumulation under tensile or relaxing tensile stress rather than under compressive or relaxing compressive stress). The current life-prediction methodology cannot distinguish between creep damage under tensile versus compressive stress states.

In the balance of this section, the elements of the existing design methodology are reviewed, the author's proposed change is detailed, the equations for implementing the change are detailed, and finally a set of four creep-fatigue tests representing two different hypothetical materials is used to illustrate how the methodology might improve life predictions. It is not the intent in this report to do an in-depth evaluation of the proposed methodology because most of the existing creep-fatigue data are proprietary or are restricted relative to publication in the open literature. The objective in this report is to present the proposed methodology and then allow others who have access to a greater body of experimental data and who are actively engaged in creep-fatigue research and development (R&D) to further evaluate the methodology

4.5.1 Current Methodology

As previously noted, the current design methodology incorporates three key elements: a damage accumulation model, a creep-fatigue interaction diagram to limit total damage, and an equivalent stress model to accommodate triaxial stresses. These elements are described in the sections that follow.

4.5.1.1 Linear Damage Model

The well-known linear damage model is based on the theory that time-under-stress results in linear accumulation of creep damage with the increments of creep damage incurred under varying loads being linearly additive. Fatigue damage is assumed to accumulate linearly with numbers of cycles, and increments of fatigue damage incurred under varying cyclic conditions are also linearly additive. The total damage is taken as the linear sum of the creep and fatigue damage sums. The Mises failure model (Mises equivalent stress) is used in these analyses to accommodate triaxial stresses. The linear damage model can be expressed as

$$D = \sum_{j=1}^{p}\left(\frac{n}{N_d}\right)_j + \sum_{k=1}^{q}\left(\frac{\Delta t}{T_r}\right)_k \tag{4.31}$$

$$D_n + D_c$$

where:

D = total creep-fatigue damage

D_n = total fatigue damage

D_c = total creep damage

n = number of applied cycles of loading condition j

N_d = number of fatigue cycles to failure under loading condition j

q = number of different time intervals with unique stress-temperature combinations required to represent the specified loading history

□t = time duration of loading condition k

T_r = creep-rupture time under loading condition k

p = number of different cyclic loading conditions with unique strain range-temperature combinations required to represent the specified loading history.

Current ASME Code Case N47 Rules[3] use a modified form of the linear damage model as shown in Figure 4.16. By placing a "knee" at the location where $D_n = D_c$, a bilinear creep-fatigue interaction diagram is formed. A design point must fall on or below the bilinear line. By moving the knee below the (0.5, 0.5) point, one can reduce the allowable damage. The location of the knee is material dependent in the code.

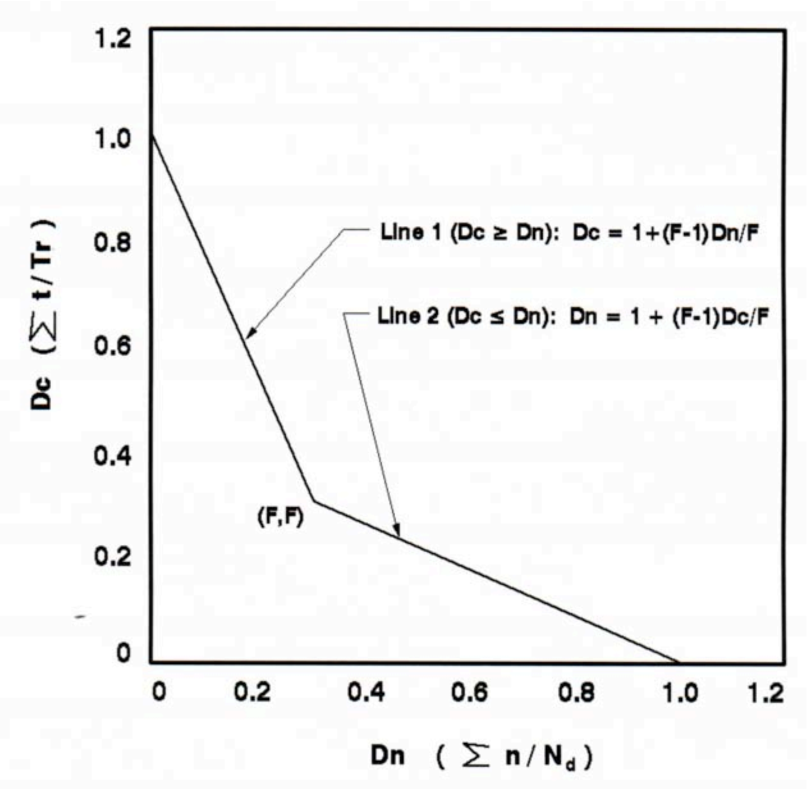

Figure 4.16. Bilinear creep-fatigue interaction diagram.

4.5.1.2 Mises Equivalent Stress Model

In the current design methodology, triaxial stress states are accommodated using the Mises equivalent stress model. Given a general stress state with principal stresses (σ_1, σ_2, σ_3), the Mises equivalent stress is defined by the equation

$$\sigma_e = \bar{\sigma} = \sqrt{\left[\left(\sigma_1 - \sigma_2\right)^2 + \left(\sigma_2 - \sigma_3\right)^2 + \left(\sigma_3 - \sigma_1\right)^2\right]/2} \tag{4.32}$$

4.5.1.3 Bilinear Creep-Fatigue Damage Interaction Diagram

In the current ASME code design methodology,[3] total creep-fatigue damage is limited by a bilinear diagram depicted in Fig. 4.16. Current ASME Code Rules define the knee in the bilinear diagram [point (F,F)] at a different location for different materials, these values being[3]:

Material	Knee (F,F)
2 1/4 Cr-1 Mo Steel	(0.1, 0.1)
Types 304 & 316 Stainless Steels	(0.3, 0.3)
Ni-Fe-Cr Alloy 800H	(0.5, 0.5)

4.5.2 Proposed Modification to Creep-Fatigue Life-Prediction Methodology

By replacing the Mises equivalent stress model in the current creep-fatigue life prediction methodology with the new H2P model, it appears that one can improve the ability of the methodology to predict life, particularly as it relates to creep damage accumulation under relaxing compressive stresses. Some materials, such as the austenitic stainless steels, tend to fail under creep-fatigue conditions by an inter-granular cracking mechanism with a tensile strain hold cycle (denoted as TEH cycle) being more damaging than a compressive strain hold cycle (denoted as CEH cycle) (i.e., when tested at the same temperature and total strain range, introducing a hold period at maximum strain [producing a relaxing tensile stress as shown in Figs. 4.17 a and b] results in a shorter life than when the same hold period is introduced at minimum strain [producing a relaxing compressive stress, as shown in Figs. 4.17 c and d]).

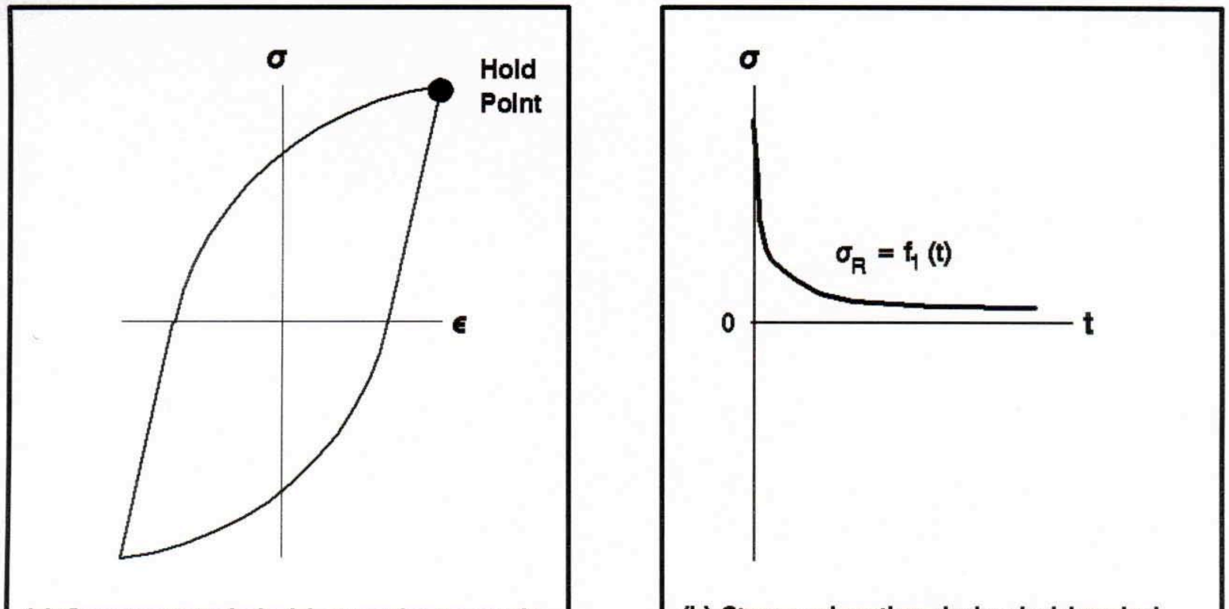
σ
Hold
Point
ϵ
σ
$\sigma_R = f_1(t)$
0
t

(a) Constant-strain hold at maximum strain (TEH cycle)

(b) Stress relaxation during hold period (TEH cycle)

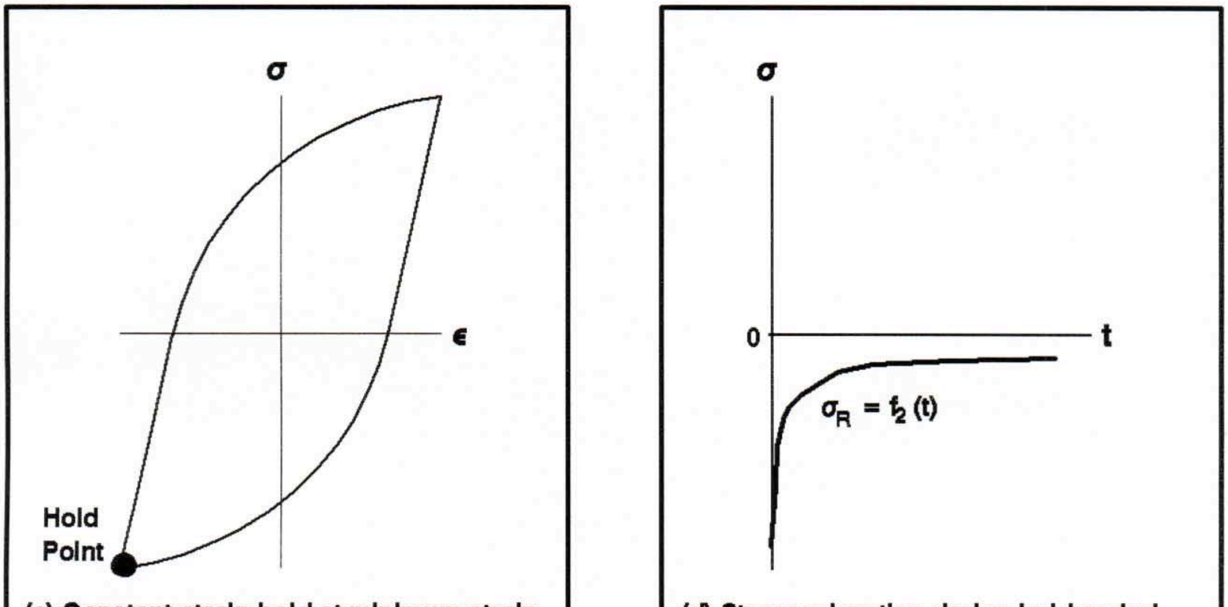
σ
ϵ
Hold
Point
σ
0
t
$\sigma_R = f_2(t)$

(c) Constant-strain hold at minimum strain (CEH cycle)

(d) Stress relaxation during hold period (CEH cycle)

Figure 4.17. Cyclic stress-strain behavior for TEH and CEH cycles.

Other materials, such as 2 1/4 Cr-1 Mo steel, when tested in air, tend to fail as a result of surface oxide cracking with the failure mechanism in general being trans-granular. For 2 1/4-Cr-1 Mo steel, the CEH cycle is more damaging than the TEH cycle. Using the existing design methodology results in equal life predictions for CEH and TEH cycles (i.e., given the same stress relaxation curve during the hold period). Replacing the Mises equivalent stress with the H2P equivalent stress allows the design methodology to more correctly predict life under CEH cycles.

For a given material, using the proposed methodology, one can determine point (F,F) on the bilinear interaction diagram from a minimum of one TEH test. One can likewise determine parameter "b" in the H2P model using a minimum of one CEH test. The observed lives for these two tests are then exactly predicted using the H2P model. However, considering the variability in creep-fatigue data, one can and should determine more appropriate values for (F,F) and "b" from a set of several TEH and several CEH tests. Determining (F,F) and "b" from multiple TEH and CEH data can easily be accomplished using a least-squares fitting approach.

Briefly stated, the proposed method includes the following:

1. Point (F,F) in the bilinear creep-fatigue interaction diagram (Fig. 4.16) is determined from uniaxial TEH creep-fatigue data.
2. The H2P equivalent stress model replaces the Mises equivalent stress.
3. Parameter "b" in the H2P equivalent stress model is determined from uniaxial CEH creep-fatigue data.
4. The linear damage model, the bilinear creep-fatigue interaction diagram, and the H2P equivalent stress model are used to predict creep-fatigue life from the stress-strain-time-temperature history produced by the applied loadings.

It is assumed that the baseline low-cycle fatigue correlation for continuous cycling of a uniaxial specimen to failure at temperature T_1 is represented by the usual equation form:

$$N_d = e\,(\Delta\varepsilon_{in})^f \tag{4.33}$$

where "e" and "f" denote material constants, $\Delta\varepsilon_{in}$ denotes the inelastic strain range, and N_d denotes the cycles to failure. This value of N_d is input into Eq. 4.31 for computing the fatigue damage fraction. Similarly, the baseline uniaxial stress-rupture correlation at temperature T_1 required in Eq. 4.31 for computing the creep-damage fraction is represented by the equation form:

$$T_r = g\,(\sigma)^h \tag{4.34}$$

where σ denotes the uniaxial stress, "g" and "h" denote material constants, and T_r denotes the time to rupture.

4.5.2.1 Bilinear Diagram Intersection Point

Two methods for determining the bilinear creep-fatigue diagram intersection point (F,F) are summarized in this report section, one method using a single TEH test and a more appropriate method using a set of several TEH tests.

Determining Bilinear Intersection Point (F,F) from a Single TEH Test: For a TEH creep-fatigue test (depicted in Fig. 4.17a and b) with a cyclic inelastic strain range, $\Delta\epsilon_{in}$, the fatigue damage per cycle, d_n , is computed using the equation:

$$d_n = 1/N_d \tag{4.35}$$

Total fatigue damage at failure, D_n , is then computed in accordance with the linear damage equation (Eq. 4.31) using the equation:

$$D_n = N_f \, d_n \tag{4.36}$$

During the constant-strain hold period, stress relaxation occurs as depicted in Fig. 4.17b, producing a time-varying stress that is characterized by the equation:

$$\sigma_R = f_1(t) \;\; >0 \text{ (tension)} \tag{4.37}$$

The stress relaxation data are collected during a laboratory test, and the half-life relaxation curve is utilized for defining $f_1(t)$ (i.e., for materials that undergo strain-hardening or strain-softening during uniaxial stress-strain cycling, the cyclic stress-strain curve changes throughout a test; hence the stress-strain curve and stress-relaxation curve at half-life are typically utilized in life predictions). Creep damage per cycle, d_c , in accordance with the linear damage model, is then determined by the equation:

$$d_c = \int_0^{t_h} \frac{dt}{T_r} \tag{4.38}$$

Combining Eqs. 4.34, 4.37, and 4.38 results in creep damage per cycle of:

$$d_c = \int_0^{t_h} \frac{dt}{\left[g\left(\left(\sigma_R\right)_e\right)\right]^h} \tag{4.39}$$

Subscript "e" on relaxation stress, σ_R , denotes that the relaxing stress is computed as the equivalent stress in accordance with the failure model (i.e., in accordance with the H2P model for the proposed methodology). The relationship between the principal stresses and the equivalent stress is the same for time-dependent creep-fatigue conditions as for time-dependent conditions. For a uniaxial tensile stress state during the relaxation period, the H2P equivalent stress (Eq. 3.7) reduces to the uniaxial tensile stress, giving:

$$\sigma_e = \bar{\sigma}\exp\left[b\left(\frac{J_1}{S_s}-1\right)\right] = \sigma_R \tag{4.40}$$

or

$$\left(\sigma_R\right)_e = \sigma_R$$

For stress relaxation under a uniaxial tensile stress state, both the H2P and the Mises equivalent stress result in $(\sigma_R)_e = \sigma_R$.

Creep damage per cycle is then determined by the equation:

$$\begin{aligned} d_c &= \int_0^{t_h}\left[\frac{dt}{g\left(\sigma_R\right)^h}\right] \\ &= \int_0^{t_h}\left[\frac{dt}{g\left[f_1(t)\right]^h}\right] \end{aligned} \tag{4.41}$$

Total creep damage at failure in N_f cycles becomes:

$$D_c = N_f\, d_c \tag{4.42}$$

The bilinear intersection point (F,F) is determined from Eq. 4.36, Eq. 4.42, and the bilinear line equations in Fig. 4.16. One must, however, determine the appropriate line (equation) in Fig. 4.16 as it relates to which is greater: fatigue or creep damage. It may be necessary to assume one is greater than the other and check this assumption when the calculation is completed. If the assumption is incorrect, it must be reversed; and the calculation repeated. These equations lead to the following solutions for "F":

Case 1: $D_c \le D_n$ ($d_c \le d_n$)

$$F = \left[\frac{D_c}{1 + D_c - D_n}\right] \tag{4.43}$$

$$= \left[\frac{N_f\, d_c}{1 + N_f d_c - N_f d_n}\right] \tag{4.44}$$

Case 2: $D_c \ge D_n$ ($d_c \ge d_n$)

$$F = \left[\frac{D_n}{1 + D_n - D_c}\right] \tag{4.45}$$

$$= \left[\frac{N_f\, d_n}{1 + N_f d_n - N_f d_c} \right] \tag{4.46}$$

If $d_c \leq d_n$, Eq. 4.44 determines the bilinear intersection point (F,F) or if $d_c \geq d_n$, then Eq. 4.46 determines the point.

Determining Bilinear Intersection Point (F,F) from Multiple TEH Tests: The better method for determining point (F,F) is to use a set of several TEH tests in conjunction with least-squares fit techniques. The following equations determine predicted life for each test:

Case 1: For $d_c \leq d_n$

$$(Np)_i = \left[\frac{F}{F d_n + (1 - F) d_c} \right]_i \tag{4.47}$$

Case 2: $d_c \geq d_n$

$$(Np)_i = \left[\frac{F}{F d_c + (1 - F) d_n} \right]_i \tag{4.48}$$

To set up the least-squares equation, let deviation, δ_i, denote the difference between predicted and observed life in an individual test “i”; then for a total of “M” tests, one can write the following m equations:

$$\delta_i = (N_p - N_f)_i \qquad i=1, M \tag{4.49}$$

The sum of the squared deviations, SSQ, becomes

$$SSQ = \sum_{i=1}^{M} \delta_i^2 \tag{4.50}$$

One can now search and determine the value of “F” that gives the minimum value for SSQ.

4.5.2.2 H2P Model Determining Parameter “b”

With a value for the bilinear intersection point (F,F) determined, parameter “b” is determined for the H2P model in a similar manner. It can be determined from a single CEH test or from a set of several CEH tests using least-squares techniques. These two methods are described below.

Determining Parameter “b” from a Single CEH Test: From a CEH creep-fatigue test conducted at temperature, T_1, the resulting data include the inelastic strain range and a stress relaxation curve (equation) during the hold period, as depicted in Figs. 4.17 c and d. The relaxing stress, as determined from laboratory data, is described by the equation:

$$\sigma_R = -f_2(t) < 0 \qquad \text{(compression)} \tag{4.51}$$

Fatigue damage during the hold period can be computed in accordance with the linear damage model (Eq. 4.31). Parameter N_d is determined by Eq. 4.33. The resulting fatigue damage per cycle and total fatigue damage at failure in N_f cycles is determined by Eqs. 4.35 and 4.36, respectively.

During the constant-strain hold period, stress relaxation occurs, producing time-varying uniaxial compressive stress determined by Eq. 4.51 with the relaxation stress, σ_R, being compressive (negative). For a uniaxial compression stress, σ, the H2P equivalent stress is:

$$\sigma_e = \bar{\sigma} \exp\left[b\left(\frac{J_1}{S_s} - 1\right)\right] = |\sigma| e^{-2b} \tag{4.52}$$

The equivalent relaxation stress, therefore, becomes

$$|\sigma_R|_e = |\sigma_R| e^{-2b} = |f_2(t)| e^{-2b} \tag{4.53}$$

Creep damage per cycle is then determined for this case by the equation:

$$\begin{aligned} dc &= \int_0^{t_h} \frac{dt}{g(\sigma_R)_e^h} \\ &= \int_0^{t_h} \frac{dt}{g\left|f_2(t) e^{-2b}\right|^h} \\ &= e^{2bh} \int_0^{t_h} \frac{dt}{g\left|f_2(t)\right|^h} \end{aligned} \tag{4.54}$$

Let "d_c" denote the creep damage per cycle, computed using the linear damage model and the H2P equivalent stress with stress relaxation defined by $\sigma_R = f_1(t) > 0$ for relaxing tensile stress and $\sigma_R = -f_2(t) < 0$ for relaxing compressive stress. Then let "d_{c1}" denote the creep damage per cycle computed using the linear damage model and H2P equivalent stress with stress relaxation defined by $\sigma_R = |f_2(t)| > 0$ for relaxing compressive stress. Damage d_{c1} thus is given by:

$$d_{c1} = \int_0^{t_h} \frac{dt}{g\left|f_2(t)\right|^h} \tag{4.55}$$

Then, from Eqs. 4.54 and 4.55, creep damage per cycle for the compression hold test becomes:

$$d_c \quad = \quad d_{c1} e^{2bh} \tag{4.56}$$

and total compressive creep damage at failure in N_f cycles becomes:

$$D_c \quad = \quad N_f \, d_{c1} e^{2bh} \tag{4.57}$$

Equations 4.56 and 4.57 show that, when the Mises equivalent stress is replaced by the H2P model equivalent stress, then for a relaxing uniaxial tensile stress both failure models compute the same creep damage. However, for a relaxing uniaxial compressive stress, creep damage computed using the H2P model is "exp(2bh)" times the damage computed using the Mises model.

Equations 4.36 and 4.57 in conjunction with the bilinear diagram equations for Lines 1 and 2 (Fig. 4.16) combine to give the following solutions for parameter "b":

Case 1: For $d_c \leq d_n$

$$b \quad = \quad \frac{1}{2h} \mathrm{Ln}\left[\frac{F\left(N_f d_n - 1\right)}{\left(F - 1\right) N_f d_{c1}}\right] \tag{4.58}$$

Case 2: For $d_c \geq d_n$

$$b \quad = \quad \frac{1}{2h} \mathrm{Ln}\left[\frac{F + \left(F - 1\right) N_f d_n}{F N_f d_{c1}}\right] \tag{4.59}$$

Depending on the relative values of d_c and d_n, one uses either Eq. 4.58 or 4.59 to determine H2P equivalent stress parameter "b" from a single CEH test and the previously determined value of "F."

Determining Parameter "b" from Multiple CEH Tests: Given a set of M CEH creep-fatigue tests, parameter "b" can be determined using a least-squares approach to give a "best fit" to the data. Fatigue and creep damage per cycle for each test is determined by Eqs. 4.35 and 4.56. Letting N_p denote predicted life for the creep-fatigue test, and then combining these two equations with the bilinear diagram equations, gives the following two equations for N_p: one for Line 1 and one for Line 2 on the bilinear diagram:

Case 1: For $d_c \leq d_n$

$$(N_p)_i \quad = \quad \left[\frac{F}{F d_n - \left(F - 1\right) d_{c1} \exp\left(2bh\right)}\right]_i \tag{4.60}$$

Case 2: For $d_c \geq d_n$

$$(N_p)_i = \left[\frac{F}{F d_{c1} \exp(2bh) - (F-1) d_n} \right]_i \tag{4.61}$$

Because the value of "b" is not known at this point, it is necessary to assume that $d_c \leq d_n$ or $d_c \geq d_n$ (individual assumption for each test) and then select the associated Eq. 4.60 or 4.61 (the assumption can be made on the basis of the known values of d_{c1} and d_n). Then, having M equations for N_p , and M values for observed N_f , the deviation, δ_i , between predicted and observed life is given by:

$$\delta_i = (N_p - N_f)_i \qquad i=1 \; M \tag{4.62}$$

with the sum of the squared deviations, SSQ, being

$$SSQ = \sum_{i=1}^{M} \delta_i^2 \tag{4.63}$$

The value of "b" giving the minimum value of SSQ is then searched and determined.

Once the best-fit value of "b" is determined, it is necessary that creep damage, d_c , be recomputed for each test using Eq. 4.56 and that one confirm the initial assumption for each of the M tests as to whether $d_c \leq d_n$ or $d_c \geq d_n$. If an incorrect assumption was made in any test, one must reverse the assumption, use the correct equation, and redetermine the value of "b."

As a second option for determining "F," a methodology for linearizing the least-squares problem is summarized in Appendix B.

4.5.3 Potential for Improved Creep-Fatigue Life Predictions

In order to illustrate the potential of the proposed design method to improve life predictions, predicted lives are compared to observed lives for two hypothetical materials. For Material 1, the TEH cycle is more damaging (results in shorter life) than the analogous CEH cycle. Materials such as the austenitic stainless steels behave in this manner. For Material 2, the CEH cycle is more damaging than the analogous TEH cycle. Materials such as 2 1/4 Cr-1 Mo steel tend to behave in this manner when tested in air. Two laboratory creep-fatigue tests of a high-temperature alloy steel are selected for Material 1 with the first test being a TEH cycle and the second being a CEH cycle. Material 2 is created as a hypothetical material with the first test chosen to be identical to the Material 1 TEH test. The second test is chosen to be identical to the Material 1 CEH test except that life is arbitrarily changed from 1345 cycles to 700 cycles to make the CEH cycle more damaging than the TEH cycle for Material 2. These "data" are summarized in Table 4.11. These values are utilized to demonstrate how the H2P model can improve life predictions when it replaces the classical Mises model in the linear-damage life prediction method. In addition to the test conditions for the four tests, computed fatigue and creep damages per cycle (dn, dc, and dc_1) are given in Table 4.11. These values are computed from the baseline low-cycle fatigue correlation for these materials (Eq. 4.33), the baseline stress rupture correlation (Eq. 4.34), and the experimental stress relaxation equations (Eqs. 4.37 and 4.51) for each test. In the interest of brevity, these data and calculations are omitted with only the damage values given. In addition to the damage values, the slope, h, of the baseline stress rupture correlation (Eq. 4.34) is required for determining H2P model parameter "b." This value is given in Table 4.11.

The data in Table 4.11 are utilized to determine the values of parameters "F" and "b" for Materials 1 and 2. The values of "F" in Table 4.11 are determined from Tests 1 and 3 with the values of "b" determined from Tests 2 and 4 for Materials 1 and 2, respectively. Because there is only one each TEH and CEH test for each material, this results in an exact fit to the data for the H2P model. The linear damage model in conjunction with the Mises equivalent stress cannot fit both the TEH and CEH tests exactly, fitting only the TEH tests. If one had multiple TEH and CEH data for a material, parameters "F" and "b" can be determined by least-squares fits to the total data set. One can then determine the degree of scatter in the resulting predictions. This is not possible with only the four tests utilized to illustrate the methodology.

Table 4.11. Creep-fatigue data utilized in demonstrating H2P failure model applicability to creep-fatigue failure prediction.

Test No.	Cycle	Test Temp. (°F)	Total Strain Range (%)	Hold Point	Hold Time (min)	Cycles to Failure	d_n	d_{c1}*	d_c*
A. Material 1 (TEH Cycle More Damaging Than CEH Cycle)									
1	TEH	1400	0.4	$\square_{max}$	2.5	1121	4.4609E–5	2.9438E–4	2.9438E–4
2	CEH	1400	0.4	$\square_{max}$	2.5	1345	4.4609E–5	2.1636E–03	1.4577E–4
B. Material 2 (CEH Cycle More Damaging Than TEH Cycle)									
3	TEH	1400	0.4	$\square_{max}$	2.5	1121	4.4609E–5	2.9438E–4	2.9438E–4
4**	CEH	1400	0.4	$\square_{max}$	2.5	700	4.4609E–5	2.1636E–3	8.3073E–4

* Slope of baseline stress rupture correlation (parameter "h," Eq. 4.35) is –6.5410 for both Materials 1 and 2.

** Test 4 is a hypothetical test with N_f arbitrarily set at 700 to create a Material 2 wherein a CEH cycle is more damaging (shorter life) than the analogous THE cycle.

For Materials 1 and 2, creep-fatigue life calculations using the linear damage model in conjunction with the H2P and the Mises models are compared in Table 4.12 showing that for the same value of "F" both the H2P and Mises models predict the same life for the TEH cycles (Tests 1 and 3); however, parameter "b" gives the H2P model the advantage of being able to exactly predict the CEH tests (Tests 2 and 4), whereas the Mises model significantly under predicts life for the CEH tests.

While overly simplistic, the comparison in Table 4.12 indicates how the H2P model may have the potential to significantly improve creep-fatigue life predictions, particularly for structures undergoing stress-strain cycling with hold periods producing compressive stresses or compressive stress relaxation. The author hopes that others actively involved in creep-fatigue R&D and/or Code Rule development will more fully evaluate the proposed method using a broader range of materials and data.

Table 4.12. A comparison of predicted and observed creep-fatigue lives based on the H2P versus the□Mises equivalent stress model.

Test No.	Cycle	Test Temp. (°F)	Total Strain Range (%)	Hold Point	Hold Time (min)	Cycles to Failure	Predicted Life (N_p) Using Linear-Damage Model With	
							H2P	Mises
A. Material 1 (TEH Cycle More Damaging Than CEH Cycle)*								
1	TEH	1400	0.4	$\square_{max}$	2.5	1121	1121	1121
2	CEH	1400	0.4	$\square_{max}$	2.5	1345	1345	362
B. Material 2 (CEH Cycle More Damaging Than TEH Cycle)**								
3	TEH	1400	0.4	$\square_{max}$	2.5	1121	1121	1121
4	CEH	1400	0.4	$\square_{max}$	2.5	700	700	362

*Test Set 1: Test 1 utilized to determine bilinear creep-fatigue diagram intersection point “F”= 0.0694 for Material 1.
Test 2 utilized to determine H2P model parameter “b” = 0.2062 for Material 1.

** Test Set 2: Test 3 utilized to determine F = 0.0694 for Material 2.
Test 4 utilized to determine b = 0.0732 for Material 2.

5.0 SUMMARY AND CONCLUSIONS

A new two-parameter failure model was developed by the author and initially reported in 1984. In 1990, after demonstrating significantly improved life predictions for creep-rupture tests of Type 304 stainless steel as compared to the classical models of Tresca, Mises, and Rankine, the two-parameter failure model, denoted as the H2P model, was incorporated into ASME Code Case N47-29[3] for the design of components operating in the elevated-temperature creep-rupture region. The objective of the current work was to evaluate the model's ability to provide improved failure predictions relative to the classical failure models of Mises, Tresca, and Rankine for both time-independent failure and time-dependent, cyclic creep-fatigue failure. This objective was met. These current assessments, in addition to the prior assessments, provide significant validation of the model for predicting time-independent fracture and time-dependent creep-rupture. A proposed method for improving life predictions for failure under time-dependent, cyclic creep-fatigue appears to have the ability to improve life predictions there as well, particularly where creep damage occurs under compressive stresses or under relaxing compressive stresses.

One can speculate on what values parameter "b" may have for material failure under time-independent fracture versus time-dependent creep-rupture and creep-fatigue. Does, for example, a material have one unique value for parameter "b?" For time-independent failure, materials having equal tensile and compressive strengths have a value of b=0.00. Many materials fall into that category. The author has conducted tests of high-strength tungsten carbide obtaining tensile strengths of 150 ksi (1,034 MPa) with a corresponding compressive strength of 950 ksi (6,550 MPa). The associated value of "b" is 0.92. Because most homogeneous materials have a compressive strength equal to or greater than the tensile strength, one can conclude that for time-independent failure of homogeneous materials, the value of "b" for essentially all materials will fall in the range from 0.0 to 0.92. Most commonly used structural materials have a ratio of compressive to tensile strength of less than 2.0, which would place the value of "b" for time-independent failure of most materials in the 0 to 0.35 range.

Insufficient data correlations have been made for creep-rupture to define or estimate the probable range in value for "b." For time-dependent creep-rupture, for the three data sets evaluated to date (Types 304 and 316 stainless steel and Inconel 600), the value of "b" has fallen in the range of 0.19 to 0.29. At this point, the author has not determined parameter "b" for different creep-fatigue data sets encompassing different materials. The data for hypothetical Material 1 in the current investigation (which was based on an actual test result) yielded a value of "b" = 0.069. This result is obviously insufficient in itself to draw any conclusions relative to the range of values one might expect in creep-fatigue tests. The idea of one value of "b" for all failure modes of a specific material, while desirable, is not likely. If, for example, one chooses to determine "b" by the ratio of compression to tensile failure strength, then in order that all failure modes have the same value of "b," the ratio of compression to tensile strength would have to be the same for all failure modes. This is not true in general.

The following specific conclusions are reached in this study:

1. The classical failure models of Mises, Tresca, and Rankine are incorporated into major structural design codes such as the ASME Code. These models have identified deficiencies, two of which are the inability to distinguish between failure under tensile versus compressive stress states and the inability to account for the effect of hydrostatic pressure on failure.

2. A new two-parameter failure model, i.e., the H2P model, has been developed and has the ability to correct the two noted deficiencies in the classical failure models. At this time there appear to be no "soft spots" in the model formulation or in the application of the model for predicting failure under any arbitrary triaxial stress state. It behaves very much like the classical Mises failure model.

3. As compared to the classical failure models, the H2P model offers the potential for significantly improved prediction of time-independent failure under a generalized triaxial stress state as demonstrated in assessments utilizing fracture data for cast iron and for marble.

4. As compared to the classical models, the H2P model has demonstrated the ability to provide significantly improved life predictions for time-dependent creep-rupture for three elevated temperature steel alloys: Types 304 and 316 stainless steels and Inconel 600.

5. The linear damage life prediction methodology utilized in ASME CCN47 for predicting life under cyclic creep-fatigue conditions was modified by replacing the Mises failure model with the H2P failure model; and it appears to have the potential to improve creep-fatigue life predictions, particularly for cyclic loadings introducing hold periods involving compressive stresses.

6.0 RECOMMENDATIONS

For the failure modes, stress states, and materials assessed to date, the H2P failure model has demonstrated the ability to more accurately predict failure under both time-independent and time-dependent failure conditions as compared to the classical failure models of Mises, Tresca, and Rankine. Additional validation of the model for a broader range of materials and triaxial stress states for both time-independent and time-dependent failure conditions would further demonstrate the model and provide additional confidence in the model's capabilities. For the important area of time-dependent, cyclic creep-fatigue, a methodology for predicting failure was outlined but is not sufficiently validated. The methodology outlined should provide life predictions similar to the Mises-based methodology for creep-fatigue cycles with tensile hold periods. The methodology has the potential to improve life predictions for cycles involving relaxing compressive stresses. However, validation of the methodology is needed, incorporating different materials and different creep-fatigue stress-strain cycles.

Finally, it is recommended that relevant ASME Code bodies evaluate the H2P failure model to determine its potential for improving existing Code rules for design against both time-independent fracture and time-dependent creep-fatigue failure.

REFERENCES

1. Timoshenko, S., *Strength of Materials,* Third Edition, D. Van Nostrand Company, Inc., New York, 1956, pp. 444–462.

2. Huddleston, R. L., "An Improved Multiaxial Creep-Rupture Strength Criterion," TRANS. ASME, Vol. 107, pp. 421–429 (1985).

3. ASME Code Case N47-29, "Class I Components in Elevated Temperature Service," Sect. III, Division 1, *Cases of ASME Boiler and Pressure Vessel Code,* American Society of Mechanical Engineers, New York, 1990.

4. Huddleston, R. L., "Assessment of An Improved Multiaxial Strength Theory Based on Creep-Rupture Data for Type 316 Stainless Steel," *ASME Journal of Pressure Vessel Technology*, Vol. 115, pp. 177–184 (May 1993).

5. Huddleston, R. L., "Assessment of An Improved Multiaxial Strength Theory Based on Creep-Rupture Data for Inconel 600," *ASME Pressure Vessel & Piping Meeting*, Denver, CO, July 26–30, 1993.

6. Pugh, H. Ll. D., "The Effect of Pressure on Fracture Stress," pp. (4)22 – (4)26 in *Recent Developments in Cold Forming*, Bulleid Memorial Lectures, Vol IIIB, University of Nottingham, 1965.

7. Chandler, E. F., *Tensile Properties of a Number of Materials Tested under Hydrostatic Pressure*, Rep. No. 306, National Engineering Laboratory, East Kilbride, Glasgow, Scotland, 1967.

8. Chandler, E. F., and Mair, W. M., "Behavior of Metals under Triaxial Compressive Stresses," pp. 122–131 in *High Pressure Engineering,* Proceedings of the Institution of Mechanical Engineers, 182, Part 3C, London, 1968.

9. Nadai, A., *Theory of Flow and Fracture of Solids*, McGraw-Hill Book Company, Inc., New York, 1950, pp. 239–244.

10. Chubb, E. J., and Bolton, C. J., "Stress State Dependence of Creep Deformation and Fracture in AISI Type 316 Stainless Steel," pp. 39–48 in *International Conference on Engineering Aspects of Creep,* September 15–19, 1980, Vol. 1, Mech. Eng. Publ. Ltd. for the Inst. of Mech. Engineers, London, 1980.

APPENDIX A. LEAST-SQUARES METHOD FOR DETERMINING H2P MODEL PARAMETER "b" FOR A SET OF M TIME-INDEPENDENT FAILURE TESTS

A least-squares-fit procedure for determining a value for H2P model parameter "b" from a set of M time-independent failure tests was derived by Merkle[1] and was provided to the author of this report along with Merkle's excellent technical review of the draft report. The procedure is summarized below and provides a relatively simple way to determine parameter "b" for this type of data.

For the H2P model, the deviation, $\square_i$, between the predicted value of stress at fracture, $\square_0$, and the observed value of stress at fracture, $\square_e$, was previously given by Eq. 3.25. For M tests, there are M equations for the deviations, $\square_i$. Because these M equations are non-linear, one cannot solve for parameter "b" outright to obtain a closed-form solution that will minimize the sum of the squared $\square_i$ deviations as previously expressed by Eq. 3.26. One can, however, convert this non-linear least-squares problem into a linear problem, then solve for parameter "b" outright. The method derived by Merkle for doing this is summarized in this appendix.

Let

$$\square_i = \square_0 - (\bar{\square})_1 \ \mathrm{Exp}\left[b\left(\left(\frac{J_1}{S_s}\right)_1 - 1 \right) \right] \tag{A.1}$$

then rearrange to get

$$\square_0 - \square_i = (\bar{\square})_1 \ \mathrm{Exp}\left[b\left(\left(\frac{J_1}{S_s}\right)_1 - 1 \right) \right] \tag{A.2}$$

$$\left(1 - \frac{\square_i}{\square_0}\right) = \frac{(\bar{\square})_1}{\square_0} \ \mathrm{Exp}\left[b\left(\left(\frac{J_1}{S_s}\right)_1 - 1 \right) \right] \tag{A.3}$$

$$\mathrm{Ln}\left(1 - \frac{\square_i}{\square_0}\right) = \mathrm{Ln}\left(\frac{(\bar{\square})_1}{\square_0}\right) + b\left(\left(\frac{J_1}{S_s}\right)_1 - 1 \right) \tag{A.4}$$

Let

$$\mu_i = \mathrm{Ln}\left(1 - \frac{\square_i}{\square_0}\right) \tag{A.5}$$

---

[1] Merkle, John G., Oak Ridge National Laboratory, P.O. Box 2008, Oak Ridge, TN 37831.

$$v_i \quad = \quad \mathrm{Ln}\left(\frac{\left(\bar{\square}\right)_i}{\square_0}\right) \tag{A.6}$$

and

$$y_i \quad = \quad \left(\frac{J_1}{S_s}\right)_i \tag{A.7}$$

Then,

$$\mu_I \quad = \quad v_I + b(y_i - 1). \tag{A.8}$$

Summing the squares of μ_i and taking the partial derivative with respect to "b" to minimize the sum of the squares gives:

$$\frac{\partial \sum_{i=1}^{M} \mu_i^2}{\partial b} \quad = \quad 0$$

$$= \quad \sum_{i=1}^{M} \left\{ \left[v_1 + b\left(y_i - 1\right) \right] \left(y_i - 1\right) \right\} \tag{A.9}$$

or

$$\sum_{i=1}^{M} v_1\left(y_i - 1\right) + b \sum_{i=1}^{M} \left(y_i - 1\right)^2 = 0 \tag{A.10}$$

Solving for "b" gives

$$b \quad = \quad -\frac{\sum_{i=1}^{M} v_1\left(1 - y_i\right)}{\sum_{i=1}^{M} \left(1 - y_i\right)^2} \tag{A.11}$$

One can now reinsert the y_i and v_i giving:

$$b \quad = \quad -\frac{\sum_{i=1}^{M} \left[\mathrm{Ln}\left(\frac{\left(\bar{\square}\right)_i}{\square_0}\right) \left(1 - \left(\frac{J_1}{S_s}\right)_i\right) \right]}{\sum_{i=1}^{M} \left(1 - \left(\frac{J_1}{S_s}\right)_i\right)^2} \tag{A.12}$$

Eq. A.12 was used to determine a least-squares fit value for parameter “b” for Pugh et al.’s time-independent failure data in Table 4.4 The resulting value was 0.440. By comparison, Eq. 3.15 was used to determine a value for “b” as an exact fit to the average of the two pure compression tests in Table 4.4. The resulting value was 0.687. A direct comparison of how well the H2P model correlates the data in Table 4.4 for the two values of “b” would be of interest; however, Merkle’s least-squares procedure for determining parameter “b” was not available until after completion of this report.

APPENDIX B. LEAST-SQUARES METHOD FOR DETERMINING H2P MODEL PARAMETER "b" FOR A SET OF M CEH-TYPE, CREEP-FATIGUE TESTS

A least-squares-fit procedure for determining a value for H2P model parameter "b" from a set of M CEH-type, creep-fatigue failure tests was derived by Merkle[1] and was provided to the author of this report along with Merkle's excellent technical review of the draft report. The procedure is summarized below and provides a relatively simple way to determine parameter "b."

Given a set of M CEH type, creep-fatigue failure tests, Eqs. 4.61 and 4.62, in conjunction with least-squares techniques are used to determine a "best fit" value for Case 1 ($d_c \leq d_n$) and Case 2 ($d_c \geq d_n$) as outlined in Section 4.0 of this report.

B.1. Case 1 ($d_c \leq d_n$):

Equation 4.61 determines the predicted life, N_p, for Case 1. This equation can be written as

$$\frac{1}{N_p} = \frac{F d_n + (1 - F) d_{c1} \mathrm{Exp}(2bh)}{F} \tag{B.1}$$

Let

$$Q = \mathrm{Exp}(2bh) \tag{B.2}$$

then, Eq. B.1 becomes

$$\frac{1}{N_p} = d_n + \left(\frac{1 - F}{F}\right) Q d_{c1} \tag{B.3}$$

Next, let

$$F' = \left(\frac{1 - F}{F}\right) \tag{B.4}$$

and insert into Eq. B.3 giving

$$\frac{1}{N_p} = d_n + F' Q d_{c1} \tag{B.5}$$

---

[1] Merkle, John G., Oak Ridge National Laboratory, P.O. Box 2008, Oak Ridge, TN 37831.

Let the deviation, δ_i , between the predicted life (cycles to failure), N_p , and the observed life, N_f , in an individual test "i" be expressed by the equation:

$$\delta_i = \frac{1}{(N_p)_i} - \frac{1}{(N_f)_i} \tag{B.6}$$

or

$$\delta_i = (d_n)_i + F \cdot Q \cdot (d_{c1})_i - \frac{1}{(N_f)_i} \tag{B.7}$$

The least-squares value for "b" is then determined by summing the squares of the M deviations for the M tests, then taking the derivative of the sum with respect to parameter Q, and then solving for Q as follows:

$$\frac{\partial\left[\sum_{i=1}^{M} \delta_i^2\right]}{\partial Q} = 0$$

$$= \sum_{i=1}^{M}\left[(d_n)_i + F \cdot Q \cdot (d_{c1})_i - \frac{1}{(N_f)_i}\right] \cdot (d_{c1})_i \tag{B.8}$$

$$\sum_{i=1}^{M}\left\{(d_{c1})_i \cdot \left[(d_n)_i - \frac{1}{(N_f)_i}\right]\right\} + Q F \cdot \sum_{i=1}^{M} (d_{c1})_i^2 = 0 \tag{B.9}$$

and solving for Q gives

$$Q = \frac{\sum_{i=1}^{M}\left\{(d_{c1})_i \cdot \left[\frac{1}{(N_f)_i} - (d_n)_i\right]\right\}}{F \cdot \sum_{i=1}^{M} (d_{c1})_i^2} \tag{B.10}$$

From Eqs. B.10 and B.2, parameter "b" is:

$$b = \frac{Ln(Q)}{2h} \tag{B.11}$$

The least-squares-fit value of H2P model parameter "b" based on a set of M CEH-type creep-fatigue tests with $d_c \leq d_n$ can be determined using Eqs. B.10 and B.11.

B.2. Case 2 ($d_c \geq d_n$):

Equation 4.62 determines the predicted life, N_p , for Case 2. This equation can be written as

$$\frac{1}{N_p} = \frac{F d_{c1} Q + (1 - F) d_n}{F} \tag{B.12}$$

or

$$\frac{1}{N_p} = Q d_{c1} + \frac{(1 - F)}{F} d_n \tag{B.13}$$

Inserting F′ from Eq. B.4 gives

$$\frac{1}{N_p} = Q d_{c1} + F' d_n \tag{B.14}$$

As in Case 1, let

$$\varepsilon_i = \frac{1}{(N_p)i} - \frac{1}{(N_f)i} \tag{B.15}$$

thus,

$$\varepsilon_i = Q(d_{c1})_i + F'(d_n)_i - \frac{1}{(N_f)_i} \tag{B.16}$$

Next, summing the squares of the deviations, ε_i , and taking the partial derivative relative to Q, and equating the sum to zero gives:

$$\frac{\partial \sum_{i=1}^{M} \varepsilon_i^2}{\partial Q} = 0$$

$$= \sum_{i=1}^{M} \left[Q(d_{c1})_i + F'Q(d_n)_i - \frac{1}{(N_f)_i} \right] (d_{c1})_i \tag{B.17}$$

or

$$Q \sum_{i=1}^{M} (d_{c1})_i^2 + \sum_{i=1}^{M} \left[(d_{c1})_i \left\{ F'(d_n)_i - \frac{1}{(N_f)_i} \right\} \right] = 0 \tag{B.18}$$

Solving for Q gives

$$Q = \frac{\sum_{i=1}^{M} \left[\left(d_{c1}\right)_i \left\{ \frac{1}{\left(N_f\right)_i} - F\left(\left(d_n\right)_i\right) \right\} \right]}{\sum_{i=1}^{M} \left(d_{c1}\right)_i^2} \qquad \text{(B.19)}$$

and then from Eq. B.2:

$$b = \frac{\mathrm{Ln}(Q)}{2h}$$

The least-squares-fit value for H2P model parameter "b" based on a set of M CEH type creep-fatigue tests with $d_c \geq d_n$ can be determined using Eqs. B.19 and B.20.

Note that a set of M tests may have some tests with $d_c \leq d_n$ and some with $d_c \geq d_n$. The procedures derived in this appendix will not work for a mixed data set of this type.

NOMENCLATURE

A_i = constants that determine which point in stress/failure space a failure model identically fits [dimensionless]

A,B,C = H2P failure surface, geometric lengths (Fig 3.1) [psi]

C = Fig. 3.5, material compressive strength [psi]

CEH = stress-strain cycle with hold point on compression side of cycle [dimensionless]

D = total damage (creep plus fatigue damage) in linear damage model [dimensionless]

D_c = total creep damage in linear damage model [dimensionless]

D_n = total fatigue damage in linear damage model [dimensionless]

F = location of "knee", (F,F), in bilinear creep-fatigue interaction diagram [dimensionless].

J_1 = 1st invariant of the stress tensor, $\square_{ij}$ [psi]

J_2 = 2nd invariant of the stress tensor, $\square_{ij}$ [psi]

J_2' = 2nd invariant of the deviatoric stress tensor, S_{ij} [psi]

M = number tests in a data set [dimensionless].

N_d = low-cycle fatigue (LCF) life computed from baseline uniaxial LCF correlation [cycles]

N_f = experimentally observed cycles to failure [cycles]

N_p = predicted cycles to failure [cycles]

P = applied hydrostatic pressure ($P \leq 0$) [psi]

S_i = deviatoric stresses for i=1,3 with $S_1 \geq S_2 \geq S_3$ [psi]

S_s = H2P model invariant stress parameter [psi]

SSQ = sum of the squared deviations of $\square_i$ in least-squares calculation [units of $\square_i^2$]

T = Fig. 3.5, material tensile strength [psi]

T = temperature [°F]

T_1 = test temperature for a specific test [°F]

T_r = creep-rupture time [hrs]

TEH = stress-strain cycle with hold point on tension side of loop [dimensionless]

W = applied torsional stress for cylindrical specimen [psi]

Z = applied axial stress for a cylindrical specimen [psi] a = H2P failure model parameter [dimensionless]

b = H2P failure model parameter [dimensionless]

c,d = Data Set 1 scaling factors for parameters $\square_{cv}$ and $\square_1$, respectively [psi/in]

d_c = creep damage per cycle computed using linear damage model and H2P equivalent stress with stress relaxation defined by $\square_R = f_1(t)>0$ for relaxing tensile stress and $\square_R = f_2(t)<0$ for relaxing compressive stress [dimensionless]

d_{c1} = creep damage per cycle computed using linear damage model and H2P equivalent stress with stress relaxation defined by $\square_R = |-f_2(t)|>0$ for relaxing compressive stress [dimensionless]

d_n = fatigue damage per cycle [dimensionless]

dt = infinitesimal time increment [hr]

e, f = baseline low-cycle fatigue equation material constants (multiplier and exponent, respectively) ["e" in cycles, "f" dimensionless]

$f_1(t)$ = time-dependent stress relaxation for a tensile hold (TEH) cycle [psi]

$f_2(t)$ = time-dependent stress relaxation for a compressive hold (CEH) cycle [psi]

g, h = baseline creep-rupture equation material constants (multiplier and exponent, respectively) ["g" in hr, "h" dimensionless]

n = linear damage model, number of applied cycles of loading condition, j [dimensionless]

p = linear damage model, number of different cyclic loading conditions with unique strain-range-temperature combinations required to represent the specified loading history [dimensionless]

q = number of different time intervals with unique stress-temperature combinations required to represent the specified loading history in linear damage model [dimensionless]

t_h = hold time in a creep-fatigue test cycle [hr]

u.v = rectangular coordinate system on creep-rupture test specimen [in.]

Greek

$\square_i$ = deviation between predicted and observed parameter value [units of parameter]

$\square_t$ = time duration of loading condition, k, in linear damage model [hr]

□ = strain [in/in]

$\square_1$, $\square_2$, $\square_3$ = principal strains in rectangular coordinates [in/in]

$\varepsilon_r, \varepsilon_\theta, \varepsilon_z$ = principal strains in cylindrical coordinates [in/in]

ε_{max} = maximum strain in a cyclic, stress-strain loop [in/in]

ε_{min} = minimum strain in a cyclic, stress-strain loop [in/in]

$\Delta\varepsilon_{in}$ = inelastic strain range [in/in]

$\Delta\varepsilon_t$ = total strain range [in/in]

σ = stress [psi]

$\bar{\sigma}$ = Mises equivalent stress [psi]

σ_{cv} = volumetric compressive stress, $J_1/3$ [psi]

σ_e = equivalent stress computed using a selected failure model [psi]

σ_i = principal stresses in rectangular coordinates (i=1,3 with $\sigma_1 \geq \sigma_2 \geq \sigma_3$) and principal stresses in cylindrical coordinates (σ_r , σ_θ , σ_z) [psi]

σ_{max} = maximum stress [psi]

σ_{min} = minimum stress [psi]

σ_R = time-dependent stress during stress relaxation [psi]

$(\sigma_R)_e$ = relaxing stress evaluated using a selected failure model equivalent stress [psi]

σ_0 = material tensile strength [psi]

σ_{0c} = material compression strength [psi]

σ_v = volumetric stress, $-J_1/3$ [psi]

σ_u, σ_v = principal stresses on a cylindrical creep-rupture specimen [psi]

τ_0 = material torsional strength [psi]

τ_{max} = maximum shear stress [psi]

Subscripts:

R = denotes stress relaxation

e = denotes that the item in brackets or parentheses is evaluated using the equivalent stress, σ_e

f = denotes parameter value at specimen failure

i,j,k = index notation, indexing integers

DISTRIBUTION

Internal Distribution

1–15	Marc Costantino	L-201
	Rich Becker	L-129
	Rich Couch	L-099
	Ian Darnell	L-228
	Dave Lassila	L-113
16	LLNL Laboratory Records Dept (RC)	
17,18	LLNL Laboratory Records Dept.	

External Distribution

Department of Energy

19 William Magwood
for Fast Reactor Program
1000 Independence Ave. SW
Washington DC 20585

20 William Magwood
for Gas-Cooled Reactor Program
1000 Independence Ave. SW
Washington DC 20585

21 William Magwood
for Pressurized Water Reactor Program
1000 Independence Ave. SW
Washington DC 20585

22 William Magwood
for Boiling Water Reactor Program
1000 Independence Ave. SW
Washington DC 20585

23 William Magwood
for Fossil Energy Program
1000 Independence Ave. SW
Washington DC 20585

24 DOE Office of Scientific and Technical Information
P.O. Box 62
Oak Ridge, TN 37831

US Nuclear Regulatory Commission

25 E. M. Hackett
RES/DET/MEB
U.S. Nuclear Regulatory Commission
Washington DC 20555-0001

26 M.T. Kirk
RES/DET/MEB
U.S. Nuclear Regulatory Commission
Washington DC 20555-0001

27 M.A. Mitchell
NRR
U.S. Nuclear Regulatory Commission
Washington DC 20555-0001

Other (USA)

28 W.H. Bamford
Westinghouse R&D Center
P.O. Box 2728
Pittsburgh, PA 15230-2728

29 Charles (Chuck) Becht
Becht Engineering Company
22 Church Street (mail: PO Box 300)
Liberty Corner, NJ 07938

30 Jarda Cervenka
Abb Lummus Global Inc
1515 Broad St
Bloomfield, NJ 07003-3002

31 S.J. Chang
Oak Ridge National Laboratory
P.O. Box 2008
Oak Ridge, TN 37831-6399

32 R.C. Cipolla
APTECH Engineering Services, Inc.
1282 Reamwood Ave.
Sunnyvale, CA 94089

33. James (Jim) Corum
2801 Staffordshire Blvd.
Powell, TN 37849

34 W.R. Corwin
Oak Ridge National Laboratory
P.O. Box 2008
Oak Ridge, TN 37831-6069

35 E. Lara-Curzio
Oak Ridge National Laboratory
P.O. Box 2008
Oak Ridge, TN 37831-6069

36 T.J. Griesbach
ATI Consulting
2010 Crow Canyon Place, Suite 140
San Ramon, CA 94583

37 Donald (Don)Griffin
208 Oakcrest Ln
Pittsburgh, PA 15236-4208

38 Benjamin (Ben) Hantz
Advanced Engrg
Exxon Research & Engrg Co
3225 Gallous Rd, Za608
Fairfax, VA 22037-0001

39-53 Roy L. Huddleston
10024 El Pinar Drive
Knoxville, TN 37922

54 Carl E. Jaske
Senior Group Leader
CC Technologies
6141 Avery Road
Dublin, OH 43016-8761

55 Maan Jawad
Nooter Corporation
Po Box 510950
Saint Louis, MO 63151-0950

56,57 Robert (Bob) Jetter
1106 Wildcat Canyon Rd.
Pebble Beach, CA 93953

58 William (Bill) Koves
UOP LLC
25 E Algonquin Rd
Des Plaines, IL 60016-6100

59 Dr. John Landes
Dept of Mechanical, Aerospace, &
Engineering Science
314 Perkins Hall
University of Tennessee
Knoxville, TN 37996

60 K.C. Liu
Oak Ridge National Laboratory
P.O. Box 2008
Oak Ridge, Tn 37831-6155

61 Noel Lobo
Secretary, Subcommittee on Materials (SC II)
for Michael Gold
Subcommittee on Materials (SC II)
Board of Pressure Technology Codes and Stds
ASME International
M/S 20S2
3 Park Avenue
New York, NY 10016

62 Edgar H. Maradiaga
Secretary, Subcommittee on Design (SC-D)
for Richard J. Basile
SubGroup on Design (SC-D)
The Boiler and Pressure Vessel Stds
Committee
Board of Pressure Technology Codes and Stds
ASME International
M/S 20S2
3 Park Avenue
New York, NY 10016

63 W. J. McAfee
Oak Ridge National Laboratory
Bldg 9204-1, MS-8047, Room 205
Oak Ridge, TN 37831

64 John G. Merkle
Oak Ridge National Laboratory
P.O. Box 2008
Oak Ridge, TN 37831-6151

65 Gerardo Moino
Secretary, High Pressure Systems Main
Committee (HPS)
for Donald M. Fryer,
Chairman, High Pressure Systems Main
Committee (HPS)
ASME International
M/S 20S2
3 Park Avenue
New York, NY 10016

66 R.K. Nanstad
Oak Ridge National Laboratory
P.O. Box 2008
Oak Ridge, TN 37831-6151

67 William J. (Bill) O'Donnell
O'donnell Consulting Engrs Inc
2940 South Park Rd
Bethel Park, PA 15102-1686

68 David (Dave) Osage
The Equity Engrg Group, Inc
3570 Warrensville Ctr Rd
Shaker Heights, OH 44122-5226

69 Janek Porowski
Jp Engrg Inc
534 Glen Arden Dr
Pittsburgh, PA 15208-2809

70 D.N. Robinson
1615 Centerview Drive
Montrose, OH 44321R.H. Dodds
University of Illinois
3140 Newmark Laboratory
205 N. Matthews
Urbana, IL 61801

71 S.T. Rosinski
Electric Power Research Institute
1300 W. Wt. Harris Blvd.
Charlotte, NC 28262-8550

72 Steven Rossi
Secretary, Subcommittee on Pressure Vessels (SC VIII)
for Urey R. Miller
SubGroup on Design (SC VIII)
Subcommittee on Pressure Vessels (SC VIII)
ASME International
M/S 20S2
3 Park Avenue
New York, NY 10016

73 Christian Sanna
Secretary, Subcommittee on Nuclear Power (SC III)
for R.P. Deubler
SubGroup on Design (SC III)
Subcommittee on Nuclear Power (SC III)
ASME International
M/S 20S2
3 Park Avenue
New York, NY 10016

74 D.A. Scarth
Ontario Hydro Research Division
800 Kipling Ave.
Toronto, Ontario
Canada M8Z5S4

75 W.L. Server
ATI Consulting
24 Grenbarr Ct.
Pinehurst, NC 28374

76 Vern Severud
3224 S. Everett Pl.
Kennewick, WA 99337-4392

77 Michael (Mike) Shelton
Parsons
1250 Cheat Rd
Morgantown, WV 26508-4125

78 M.A. Sokolov
Oak Ridge National Laboratory
P.O. Box 2008
Oak Ridge, TN 37831-6151

79 Robert W. Swindeman
Oak Ridge National Laboratory
P.O. Box 2008
Oak Ridge, TN 37831-6155

80 Dr. Y. J. Weitsman
Dept of Mechanical, Aerospace, & Engineering Science
307 Perkins Hall
University of Tennessee
Knoxville, TN 37996-2030

81 P.T. Williams
Oak Ridge National Laboratory
P.O. Box 2009
Oak Ridge, TN 37831-8056

82 K.K. Yoon
Framatome Technologies
3315 Old Forest Road
P.O. Box 10935
Lynchburg, VA 24506-0935

83 S.J. Zinkle
Oak Ridge National Laboratory
P.O. Box 2008
Oak Ridge, TN 37831-6138

FOREIGN

84 Tai Asayama
Japan Nuclear Cycle Development Institute
Oarai Engineering Center
4002 Narita, Oarai, Higashi-Ibaraki,
Ibaraki, 311-1393, Japan

85 Dr. Koji Iwata
1-65 Keyakidai
Mito, Ibaraki-ken
310-0842 JAPAN